

RADIATIVE GRAIN ALIGNMENT IN PROTOPLANETARY DISKS: IMPLICATIONS FOR POLARIMETRIC OBSERVATIONS

RYO TAZAKI^{1,2}, ALEXANDRE LAZARIAN³, AND HIDEKO NOMURA²

Accepted for publication in ApJ

ABSTRACT

We apply the theory of radiative torque (RAT) alignment for studying protoplanetary disks around a T-Tauri star and perform 3D radiative transfer calculations to provide the expected maps of polarized radiation to be compared with observations, such as with ALMA. We revisit the issue of grain alignment for large grains expected in the protoplanetary disks and find that mm-sized grains at midplane do not align with magnetic field as the Larmor precession timescale for such large grains becomes longer than the gaseous damping timescale. Hence, for these grains the RAT theory predicts that the alignment axis is determined by the grain precession with respect to the radiative flux. As a result, we expect that the polarization will be in the azimuthal direction for a face-on disk. It is also shown that if dust grains have superparamagnetic inclusions, magnetic field alignment is possible for (sub-)micron grains at the surface layer of disks, and this can be tested by mid-infrared polarimetric observations.

Keywords: dust, extinction — polarization — protoplanetary disks — radiative transfer

1. INTRODUCTION

Magnetic fields play an important role in accretion disks at different stages. In particular, at the initial stages of disk formation, they have been proposed as a cause of the “magnetic breaking catastrophe” that can prevent the disks from forming. Different ideas about how to resolve this problem have so far been considered (e.g., Li et al. 2014), and the most promising scenario is the reconnection diffusion (Lazarian 2005, 2014) driving the magnetic fields out (see González-Casanova et al. 2016). At later stages the magneto-rotational instability (Velikhov 1959; Chandrasekhar 1960; Balbus & Hawley 1991) can play an important role in the driving the accretion. The presence of turbulence affects not only gas dynamics, but also grain dynamics. In the disk, micron-sized dust grains coagulate to form cm-sized dust aggregates, and this finally gives rise to the formation of planetesimals. However, high-speed collisions between grains excited by disk turbulence often result in fragmentation; thereby, turbulence may halt the planetesimal formation. For these reasons, it is important to constrain the magnetic field strength and structure by observations.

Mid-infrared and millimeter polarimetric observations has so far been considered as the best method to probe the magnetic field. This is because if aspherical grains in disks become aligned with the magnetic field as is the case in the interstellar medium (ISM), the polarization vector arising from thermal emission of the aligned grains becomes perpendicular to the local magnetic field line (Cho & Lazarian 2007, henceforth CL07; Yang et al. 2016b; Matsakos et al. 2016; Bertrang et al. 2017). At mid-infrared wavelengths, Li et al. (2016) performed a polarimetric imaging observation of AB Aur using CanariCam. As a result, they detected a centrosymmetric polarization pattern, and the degree of polarization was

as high as 1.5% at large radii. At millimeter wavelengths, polarimetric observations of disks have been performed so far (e.g., Hughes et al. 2009; Hughes et al. 2013; Cox et al. 2015; Rao et al. 2014; Stephens et al. 2014; Kataoka et al. 2016b). Polarized emission from a circumstellar disk has been detected in the Class 0 phase (Cox et al. 2015; Rao et al. 2014). More evolved disks do not show a degree of linear polarization larger than 0.5% (Hughes et al. 2009; Hughes et al. 2013). It should be mentioned that Stephens et al. (2014) detected polarized flux from HL Tau, which is classified as a Class I-II, with an average degree of linear polarization of 0.9%. More recently, Kataoka et al. (2016b) reported the first submillimeter polarization observation of a disk obtained with ALMA, and they clearly detected polarized flux from HD 142527. The polarization fraction at a peak position of polarized intensity was 3.26%, and a maximum polarization fraction was as high as 13.9%. The disk reveals radial polarization vectors; however, they flips by 90° in its northeast and northwest regions. In addition, the detected polarization fraction is much larger than the stringent limit set by Hughes et al. (2009) and Hughes et al. (2013), and further polarimetric observations by ALMA will reconcile this discrepancy.

Theoretically, the origin of mid-infrared and millimeter polarization of protoplanetary disks is still a matter of debate. In the disk, polarized radiation is expected to arise from (i) the thermal emission of aligned aspherical grains (CL07) and/or (ii) the scattering of an anisotropic radiation field by dust grains (Kataoka et al. 2015, 2016a; Yang et al. 2016a,b; Pohl et al. 2016). CL07 studied grain alignment in a protoplanetary disk and they concluded that a polarization fraction of 2-3 % at (sub-)millimeter wavelength can be expected. Since the magnetic field of disks is dominated by the toroidal field, grain alignment in disks has been considered to produce a radial polarization vector for a face-on disk (Yang et al. 2016b; Matsakos et al. 2016; Bertrang et al. 2017). Scattering polarization can be important when the maximum grain size in disks is similar to the observing wavelength (Kataoka et al. 2015), and a disk inclination also helps to produce the polarized radiation by the scattering (Yang et al. 2016a,b). A scattering polarization vector for the scattering basically traces

¹ Department of Astronomy, Graduate School of Science, Kyoto University, Kitashirakawa-Oiwake-cho, Sakyo-ku, Kyoto 606-8502, Japan; rtazaki@kusastro.kyoto-u.ac.jp

² Department of Earth and Planetary Sciences, Tokyo Institute of Technology, 2-12-1 Ookayama, Meguro-ku, Tokyo 152-8551, Japan

³ Department of Astronomy, University of Wisconsin, Madison, WI 53706, USA

the radiative flux, i.e., for a smooth face-on disk, a polarization vector will be in the azimuthal direction.

In this paper, we revisit grain alignment in disks since the work of CL07 was published before a theory of radiative torque (RAT) alignment had been formulated, i.e. before the RAT alignment paper of Lazarian & Hoang (2007, henceforth LH07). Taking into account present-day RAT alignment theory (see the review by Lazarian et al. 2015) may largely impact on their results. Major updates of the RAT alignment theory after CL07 are as follows. Firstly, CL07 adopted an alignment condition based on Draine & Weingartner (1996); however, LH07 showed that their condition does not express the onset of grain alignment correctly. Secondly, CL07 assumed dust grains always become aligned with the magnetic field when the alignment condition is satisfied. However, mm-sized grains are more likely to be aligned with the radiation direction rather than with the magnetic field due to their relatively slow Larmor precession in the magnetic field (LH07, Lazarian & Hoang in preparation). Thirdly, CL07 assumed perfect internal alignment, while all mechanisms of internal alignment become inefficient for sufficiently large grains (Purcell 1979; Lazarian & Draine 1999; Lazarian & Efrimsky 1999; Lazarian & Hoang 2008). In the absence of internal alignment, grain alignment is still possible; however, the degree of alignment, and hence the degree of polarization, is reduced (Hoang & Lazarian 2009a).

This paper is organized as follows. In Section 2, we describe our model of radiative grain alignment. In Section 3, a disk model and dust models we use in the calculations are summarized. In Section 4, the proper alignment axis in the disk is presented based on the radiative transfer calculations and a timescale argument. In Section 5, we estimate the degree of polarization from the disk. In Section 6 we discuss implications for the observations, and our conclusions are presented in Section 7.

2. MODEL OF GRAIN ALIGNMENT

In this section, we state our model for grain alignment. In Section 2.1, we summarize the RAT alignment process. In Section 2.2, we describe the essential timescales for RAT alignment. In Section 2.3, based on these timescales given in Section 2.2, we summarize the alignment conditions.

2.1. Overview of RAT alignment

In general, grain alignment involves two different alignment processes (see also Figure 1): (1) alignment of the angular momentum vector of the grains with the magnetic field ($\xi \rightarrow 0$) or alignment of the angular momentum vector of grains with the direction of the anisotropic radiation ($\Theta \rightarrow 0$), and (2) alignment of the minor axis of the grains with the angular momentum vector ($\theta \rightarrow 0$). These alignment processes are referred to as *external alignment* and *internal alignment*.

The driving physics of external alignment is RAT. RAT alignment naturally explains the observed features of the interstellar polarization (see the review by Andersson et al. 2015). The presence of RAT was firstly realized by Dolginov & Mitrofanov (1976) and confirmed by numerical simulations by Draine & Weingartner (1996, 1997). Draine & Weingartner (1996) found that RAT under the isotropic radiation can spin up a grain suprathermally, and the subsequent paramagnetic dissipation (Davis & Greenstein 1951) leads to grain alignment with respect to the magnetic field. However, RAT arising from the isotropic radiation is fixed in grain coordinates and this prevents grains from

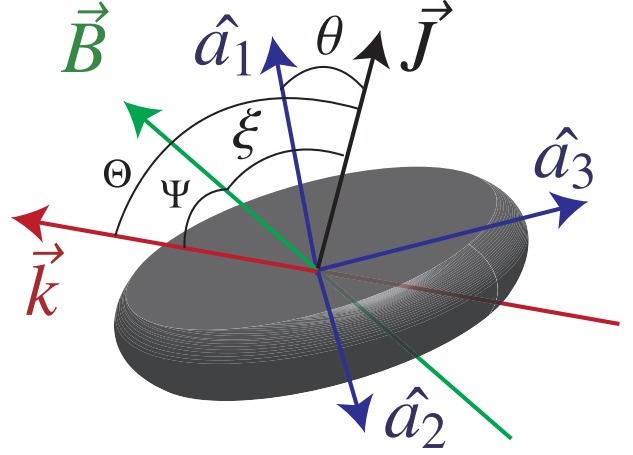


Figure 1. Definition of the coordinate system. \hat{a}_1 is the short axis of the grain, and \hat{a}_2 and \hat{a}_3 corresponds to the long axis of the grain. \mathbf{J} is the angular momentum vector of the grain. \mathbf{B} is the local magnetic field and \mathbf{k} is the direction of the anisotropic radiation field, or simply the direction of the radiative flux.

rotating suprathermally due to the effect known as thermal flipping (Lazarian & Draine 1999; Hoang & Lazarian 2009b). Draine & Weingartner (1997) argued that dust grains can be spun up to suprathermal under an anisotropic radiation field. In addition, they also found that in this case, RAT can drive external alignment even in the absence of paramagnetic dissipation. However, calculations taking into account a more accurate treatment of crossover⁴ showed that RAT under an anisotropic radiation field often spin down the grain rotation to thermal or subthermal (Weingartner & Draine 2003; LH07). An important property of RAT alignment is that a system of dust grains evolves into stable points in the parameter space of the angular momentum and the alignment angle. These stable points are often referred to as the “attractors” (Draine & Weingartner 1997). They often (but not always) appear at perfect alignment i.e., $\xi = 0$ and $\Theta = 0$ (Draine & Weingartner 1997; LH07). There exist two kinds of attractors: one is high- J attractors (a spin-up state) whose angular momentum is suprathermal, and the low- J attractors (a spin-down state) whose angular momentum is thermal or subthermal. High- J and low- J attractors can appear simultaneously in the phase trajectory map; however, even in this case, only a small fraction of grains reaches to the high- J attractor. For this reason, it turns out that suprathermal rotation driven by RAT should not be used as a necessary condition for the alignment (see also the review by Lazarian 2007). It is worth noting that the appearance of high- J or low- J attractors can be predicted by the q^{\max} -parameter and Ψ (see Figure 24 of LH07), where the q^{\max} -parameter describes the grain morphology, or the grain helicity.

A necessary condition of RAT alignment is the precession motion of a grain. This is essential for grain alignment because the precession axis defines the alignment axis regardless of the origin of precession. If dust grains are forced to quit precession due, for example, to the gaseous damping, alignment does not occur. This is because the grain precession motion can stabilize the alignment torque. The major origin of grain precession is Larmor precession or radia-

⁴ Disregard of the crossover physics resulted in the appearance of cyclic phase trajectories in Draine & Weingartner (1997) and Weingartner & Draine (2003). This cyclic behavior is not physical. Instead, the grains enter the low- J attractor point (Weingartner & Draine 2003; LH07).

tive precession (see Section 2.2 for more details). If Larmor precession governs the grain precession motion, dust grains become aligned with the magnetic field, as is the case in the ISM. On the other hand, if radiative precession overcomes Larmor precession, grains become aligned with the direction of radiation, not the magnetic field (LH07). The above basic physics should be augmented by additional important points. First of all, the grain alignment at the high- J attractor point can be stabilized by enhanced magnetic susceptibility arising from superparamagnetic or ferromagnetic inclusions, e.g. iron clusters (Lazarian & Hoang 2008; Hoang & Lazarian 2016). The latter alignment is perfect, unlike the result for low- J alignment, which does not usually exceed 30% (Hoang & Lazarian 2008). In addition, suprathermal torques introduced originally by Purcell (1979), if present in circumstellar disks, can also increase the degree of RAT alignment (Hoang & Lazarian 2009b).

Internal alignment, or internal relaxation, is a process where the grain axis for the maximum inertia aligns with the angular momentum vector (Purcell 1979). The rotational kinetic energy of a body can be given by (see Lazarian & Roberge 1997)

$$E(\theta) = \frac{J^2}{I_{\parallel}}(1 + \sin^2 \theta(h - 1)), \quad (1)$$

where $h = I_{\parallel}/I_{\perp}$, I_{\parallel} and I_{\perp} represent the inertia with respect to the grain minor axis and major axis, J is the angular momentum of the grain, and θ is the angle between $\hat{\mathbf{a}}_1$ and \mathbf{J} . The rotational kinetic energy of a body can be converted into heat by internal energy dissipation. Since the angular momentum of a body J is conserved when we consider torque-free motion of a rigid body, energy dissipation leads to alignment of the axis of the greatest inertia of the grains with its angular momentum vector. Various energy dissipation processes have so far been proposed: Barnett relaxation (Purcell 1979), nuclear relaxation (Lazarian & Draine 1999), superparamagnetic Barnett relaxation (Lazarian & Draine 1999; Hoang & Lazarian 2008), and inelastic relaxation (Purcell 1979; Lazarian & Efroimsky 1999).

2.2. Timescales relevant to RAT alignment

In this study, we use the timescales to specify the degree of grain alignment instead of solving the equation of motion of an aspherical grain under an anisotropic radiation field. We summarize the relevant timescales of external alignment and internal alignment.

2.2.1. Grain geometry

Modeling of the interstellar polarization has been suggested that an oblate grain is preferred to a prolate grain (Lee & Draine 1985; Henning & Stognienko 1993; Kim & Martin 1995; Hildebrand & Dragovan 1995). In addition, Hildebrand & Dragovan (1995) showed that an oblate with axis ratio of 2:3 produces the best fit for far-infrared polarization. Although dust grains in disks may differ from interstellar grains, in this paper, we adopt an oblate spheroid for simplicity. Denoting the inertia with respect to the grain minor axis and major axis by I_{\parallel} and I_{\perp} , respectively, then

$$I_{\parallel} = \frac{8\pi}{15}\rho_s a_1 a_2^4, \quad I_{\perp} = \frac{4\pi}{15}\rho_s a_1 a_2^2(a_1^2 + a_2^2), \quad (2)$$

where ρ_s is the material density, a_1 , a_2 denotes the minor and major radii of a grain, and then the grain aspect ratio s

is defined by $s = a_1/a_2$. It is useful to define a characteristic radius of an aspherical grain. In this paper, we use the volume-equivalent radius a_{eff} for which the volume of sphere with radius a_{eff} equals to that of the original ellipsoid; hence, $a_{\text{eff}}^3 \equiv a_1 a_2^2$.

2.2.2. Gaseous damping timescale

Random collisions of gas particles prevents grains from being aligned. Roberge et al. (1993) derived the gaseous damping timescale assuming perfect sticking of colliding molecules and subsequent evaporation of molecules from the surface, which are assumed to be thermalized at the grain surface. Although the mean torque due to sticking collision is canceled out, that due to evaporation is non-zero for spinning grains. Thus, evaporated molecules extract angular momentum from spinning dust grains. The timescale for which grain angular momentum becomes zero via the gaseous damping is given by

$$t_{\text{gas}} = \frac{3}{4\sqrt{\pi}} \frac{I_{\parallel}}{\rho_g v_{\text{th}} a_2^4 \Gamma_{\parallel}} \quad (3)$$

$$\approx 8.1 \times 10^{-3} \hat{\rho}_s a_{-5} \hat{\rho}_g^{-1} \hat{T}_g^{-1/2} \text{ yr} \quad (4)$$

where ρ_g is the gas density, T_g is the gas temperature, ρ_s is the material density, $v_{\text{th}} = \sqrt{2k_B T_g / \mu m_H}$, where $\mu = 2.34$ is a mean molecular weight. Γ_{\parallel} is a geometrical coefficient given by

$$\Gamma_{\parallel} = \frac{3}{16} \{3 + 4(1 - e_m^2) \tilde{g}(e_m) - e_m^{-2} [1 - (1 - e_m^2)^2 \tilde{g}(e_m)]\} \quad (5)$$

$$\tilde{g}(e_m) = \frac{1}{2e_m} \ln \left(\frac{1 + e_m}{1 - e_m} \right) \quad (6)$$

where $e_m^2 = 1 - s^2$. We adopt the following normalization: $\hat{\rho}_s = \rho_s / 3 \text{ g cm}^{-3}$, $\hat{s} = s / 0.5$, $a_{-5} = a_{\text{eff}} / 10^{-5} \text{ cm}$, $\hat{\rho}_g = \rho_g / 10^{-15} \text{ g cm}^{-3}$, $\hat{T}_g = T_g / 100 \text{ K}$. Note that we disregard infrared emission damping (Purcell & Spitzer 1971) and the plasma drag (Draine & Lazarian 1998), because this mechanism only becomes important for small grains whose size is less than $0.1 \mu\text{m}$, while we expect more larger grains in disks.

2.2.3. Precession of \mathbf{J} around \mathbf{B} : Larmor precession timescale

A magnetized body precesses around an applied magnetic field, and this is called Larmor precession. Even in the absence of a spontaneous magnetic moment, spinning dust grains can acquire a magnetic moment via (i) surface charges (Martin 1971) and (ii) the Barnett effect (Dolginov & Mitrofanov 1976). If a dust grain has non-zero surface charges, the spinning grain generates a magnetic dipole moment via the surface current, and hence the grain becomes magnetized. The Barnett effect⁵ is a phenomenon in which a rotating body becomes magnetized with the magnetic moment parallel to the angular velocity (Barnett 1915). In most cases, a magnetic moment induced by grain rotation is dominated by the Barnett effect. Thus, in this paper, we neglect the magnetization by surface charges.

The Larmor precession timescale, or the timescale of precession of the magnetic moment induced by grain rotation

⁵ The Barnett effect is a reciprocal phenomenon of the Einstein-de Haas effect in which magnetization of a body induces mechanical rotation (see, e.g., Landau & Lifshitz 1960).

around the magnetic field B can be given by

$$t_L = \frac{2\pi}{\Omega_L}, \quad \Omega_L = \frac{\mu_{\text{Bar}} B}{I_{\parallel} \omega} \quad (7)$$

where Ω_L is the angular frequency of Larmor precession, ω is the angular frequency of a grain rotation, and μ_{Bar} is the magnetic moment induced by the Barnett effect (Landau & Lifshitz 1960):

$$\mu_{\text{Bar}} = \frac{\chi(0)V\hbar}{g\mu_B} \omega \quad (8)$$

where V is the volume of the grain, \hbar is the Planck constant divided by 2π , and $\mu_B = e\hbar/2m_e c \approx 9.274 \times 10^{-21}$ erg G $^{-1}$ is the Bohr magneton, where m_e is the mass of the electron, and c is the speed of light, and g is the g -factor, which is $g \approx 2$ for electrons. $\chi(0)$ is the magnetic susceptibility at zero frequency. From Equations (7) and (8), we obtain

$$t_L = \frac{4\pi}{5} \frac{g\mu_B}{\hbar} \rho_s s^{-2/3} a_{\text{eff}}^2 B^{-1} \chi(0)^{-1} \quad (9)$$

$$\approx 1.3 \hat{\rho}_s \hat{s}^{-2/3} a_{-5}^2 \hat{B}^{-1} \hat{\chi}^{-1} \text{ yr} \quad (10)$$

where $\hat{B} = B/5 \mu\text{G}$, $\hat{\chi} = \chi(0)/10^{-4}$.

The magnetic susceptibility of dust grains depends on the grain's material properties. Most materials have unpaired electrons in the outer, partly filled shell, and these electrons can contribute to the grain magnetic moment. If the interaction between spins can be ignored, the material is regarded as paramagnetic. A property of paramagnetic grains is that in the absence of an applied magnetic field, the number of up-spins and down-spins is statistically the same; hence, a paramagnetic material does not have a spontaneous magnetic moment. However, once the field is applied, it becomes magnetized. Suppose f_p is the fraction of atoms in the grain that are paramagnetic; then the zero-frequency susceptibility is given by the Curie's law (Morrish 2001),

$$\chi(0) = \chi_e(0) = 4.2 \times 10^{-2} f_p \left(\frac{T_d}{15 \text{ K}} \right)^{-1} \quad (11)$$

As the grain temperature increases, the spin thermal fluctuation of spins halts the magnetization, and then the magnetic susceptibility is reduced. Observations of interstellar depletion suggest that 10% of grain atoms are Fe atoms; then f_p is as large as 0.1 (e.g., Draine 1996). Jones & Spitzer (1967) proposed that the magnetic susceptibility of grains can be largely enhanced by the presence of superparamagnetic inclusions. An example of a superparamagnetic inclusion is a nanocluster of iron atoms. Iron atoms in a cluster interact with neighboring atoms by an exchange interaction such as ferromagnetism, and then a single cluster behaves as if it were a single atom having a large magnetic moment. As a result, this grain behaves as if it were ferromagnetic under the presence of an applied field. The volume of the cluster is small enough such that its magnetic moment of a single cluster readily flips due to thermal fluctuation; therefore, a superparamagnetic grain does not have a spontaneous magnetic moment. Hence, dust grains with superparamagnetic inclusions behaves like paramagnetic grains in the absence of an applied field, and ferromagnetic grains in the presence of the field. The zero-frequency susceptibility for a superparamagnetic grain is given by the Curie's law (Morrish 2001),

$$\chi(0) = \chi_{\text{sup}}(0) = 1.2 \times 10^{-2} N_{\text{cl}} \phi_{\text{sp}} \left(\frac{T_d}{15 \text{ K}} \right)^{-1}, \quad (12)$$

where ϕ_{sp} is the fraction of atoms that are superparamagnetic. N_{cl} is the number of atoms per cluster. The typical value from measurement of GEMS suggests $\phi_{\text{sp}} = 0.03$ (Bradley 1994; Martin 1995), and N_{cl} is expected to have $N_{\text{cl}} = 10^3 - 10^5$ (Jones & Spitzer 1967).

2.2.4. Precession of \mathbf{J} around \mathbf{k} : Radiative precession timescale

When dust grains are immersed in an anisotropic radiation field, they experience RAT. The role of RAT is give rise to spin up (down), alignment, and to induce grain precession. LH07 identified RAT alignment with respect to the radiative flux rather than the magnetic field in the situations where the grain precession rate induced by RAT exceeds that induced by Larmor precession. The RAT is defined by (Draine & Weingartner 1996)

$$\Gamma_{\text{rad}} = \frac{u_{\text{rad}} a_{\text{eff}}^2 \bar{\lambda}}{2} \bar{\gamma} \overline{\mathbf{Q}_R} \quad (13)$$

where a bar indicates the spectrum-averaged quantities,

$$\overline{\mathbf{Q}_R} = \frac{\int \mathbf{Q}_R u_{\lambda} d\lambda}{u_{\text{rad}}}, \quad \bar{\lambda} = \frac{\int u_{\lambda} \lambda d\lambda}{u_{\text{rad}}}, \quad (14)$$

$$\bar{\gamma} = \frac{\int u_{\lambda} \gamma_{\lambda} d\lambda}{u_{\text{rad}}}, \quad u_{\text{rad}} = \int u_{\lambda} d\lambda \quad (15)$$

where u_{λ} is the energy spectrum of the radiation field, λ is the radiation wavelength, γ_{λ} is the anisotropy parameter, and \mathbf{Q}_R is the RAT efficiency. The amplitude of \mathbf{Q}_R is estimated by the DDA calculation (LH07),

$$|\mathbf{Q}_R| \approx 2.3 \left(\frac{\lambda}{a_{\text{eff}}} \right)^{-3} \quad \text{for } \lambda > 1.8 a_{\text{eff}} \quad (16)$$

$$\approx 0.4 \quad \text{for } \lambda \leq 1.8 a_{\text{eff}} \quad (17)$$

The radiative precession timescale can be written as (LH07)

$$t_{\text{rad, p}} = \frac{2\pi}{\Omega_p}, \quad (18)$$

$$\Omega_p = \frac{u_{\text{rad}} \bar{\lambda} a_{\text{eff}}^2}{I_{\parallel} \omega} \gamma |\overline{\mathbf{Q}_R}| \quad (19)$$

where I_{\parallel} is the maximum moment of inertia, and ω is the angular velocity of a grain.

$$t_{\text{rad, p}} \approx 1.1 \times 10^2 \hat{\rho}_s^{1/2} \hat{s}^{-1/3} a_{-5}^{1/2} \hat{T}_d^{1/2} \times \left(\frac{u_{\text{rad}}}{u_{\text{ISRF}}} \right)^{-1} \left(\frac{\bar{\lambda}}{1.2 \mu\text{m}} \right)^{-1} \left(\frac{\gamma |\overline{\mathbf{Q}_R}|}{0.01} \right)^{-1} \text{ yr}, \quad (20)$$

where we have assumed the thermal angular velocity $\omega = \sqrt{2k_B T_d / I_{\parallel}}$.

2.2.5. Internal alignment timescale

To estimate the internal alignment timescale, we assume the torque-free motion. As we discussed in Section 2.2.2, gas particles exerts torque on dust grains; hence, an approximation of the torque-free motion is valid when we consider a timescale shorter than that of the gaseous damping. The timescale for

⁶ There is a typographical error in their Equation (85).

internal alignment is given by (Purcell 1979; Roberge et al. 1993; Lazarian & Roberge 1997),

$$t_{\text{int}} = G \frac{\gamma^2}{K(\omega)}, \quad G = \frac{I_{\parallel}^3}{h^2(h-1)VJ_T^2} \left(\frac{J_T}{J} \right)^2 \quad (21)$$

where γ is the gyromagnetic ratio, and $J_T = \sqrt{I_{\parallel} k_B T_d / (h-1)}$ is the thermal angular momentum of the grains. K is the ratio of the imaginary part of the magnetic susceptibility and frequency:

$$K \equiv \frac{\chi''}{\omega} = \chi(0) \frac{\tau}{[1 + (\omega\tau/2)^2]^2} \quad (22)$$

where τ is the timescale of the relaxation (Morrish 2001). Note that the integration of $K(\omega)$ over zero frequency to infinity gives simply give $\chi(0)$ because of the requirement of the Kramers-Krönig relationship (e.g., Landau & Lifshitz 1960). As energy dissipation proceeds, the minor axis of the grains becomes aligned with its angular momentum vector. The following relaxation mechanisms can be considered: Barnett relaxation, nuclear relaxation, superparamagnetic Barnett relaxation, and inelastic relaxation. The timescale for each process can be estimated as described below.

Barnett relaxation (Purcell 1979) is due to relaxation of the electron's spin-spin interaction. Hence, the gyromagnetic ratio in Equation (21) is given by the electron, then

$$\gamma = \gamma_e = \frac{\mu_e}{\hbar} = \frac{g_e \mu_B}{\hbar}, \quad (23)$$

where $g_e \approx 2$, and $\mu_B = e\hbar/2m_e c$ is the Bohr magneton. $\tau = \tau_e = 2.9 \times 10^{-12} f_p^{-1}$ s is the spin-spin coupling time (Morrish 2001). Using Equations (21), (22), (23), and (11), we obtain the timescale for internal alignment due to Barnett relaxation as

$$t_{\text{Bar}} \equiv G \frac{\gamma_e^2}{K_e} \quad (24)$$

$$\approx 2.3 \hat{\rho}_s^2 a_{-5}^7 \left(\frac{J_T}{J} \right)^2 \left[1 + \left(\frac{\omega\tau_e}{2} \right)^2 \right]^2 \text{ yr.} \quad (25)$$

Lazarian & Draine (1999) found that the nuclear-electron spin interaction and nuclear-nuclear spin interaction lead to dissipation of the energy and this gives rise to internal relaxation. In the case of nuclear relaxation,

$$\gamma = \gamma_n = \frac{\mu_n}{\hbar} = \frac{g_n \mu_N}{\hbar}, \quad (26)$$

where $\mu_N = e\hbar/2m_p c$ is the nuclear magneton and m_p is the mass of the proton. The zero-frequency susceptibility is given by the Curie's law (Morrish 2001),

$$\chi(0) = \chi_n(0) = 4.1 \times 10^{-11} \left(\frac{\mu_n}{\mu_N} \right)^2 \left(\frac{n_n}{10^{22} \text{ cm}^{-3}} \right) \left(\frac{T_d}{15 \text{ K}} \right)^{-1}. \quad (27)$$

The relaxation timescale of nuclear spin is given by $\tau_n^{-1} = \tau_{nn}^{-1} + \tau_{ne}^{-1}$, where the timescales for nuclear-electron spin and nuclear-nuclear spin interactions are described by

$$\tau_{ne} = 3.0 \times 10^{-4} \left(\frac{2.7}{g_n} \right)^2 \left(\frac{n_n}{10^{22} \text{ cm}^{-3}} \right) \quad (28)$$

$$\tau_{nn} = 0.58 \tau_{ne} \left(\frac{n_e}{n_n} \right), \quad (29)$$

respectively (Lazarian & Draine 1999). As a result,

$$t_{\text{nuc}} \equiv G \frac{\gamma_n^2}{K_n} \quad (30)$$

$$\approx 4.6 \times 10^{-6} \hat{\rho}_s^2 a_{-5}^7 \left(\frac{J_T}{J} \right)^2 \left[1 + \left(\frac{\omega\tau_n}{2} \right)^2 \right]^2 \text{ yr} \quad (31)$$

In the presence of superparamagnetic inclusions, superparamagnetic Barnett relaxation is important. For this process, the gyromagnetic ratio is given by $\gamma = \gamma_e$. The relaxation timescale is

$$\tau_{\text{sup}}^{-1} = \nu_0 e^{-N_{\text{cl}} \theta / T} \quad (32)$$

where $\nu_0 = 10^9 \text{ s}^{-1}$, and $\theta = 0.011 \text{ K}$ (Morrish 2001). As a result,

$$t_{\text{sup}} \equiv G \frac{\gamma_e^2}{K_{\text{sup}}} \quad (33)$$

$$\approx 4.2 \times 10^{-4} \hat{\rho}_s^2 a_{-5}^7 \left(\frac{J_T}{J} \right)^2 \left[1 + \left(\frac{\omega\tau_{\text{sup}}}{2} \right)^2 \right]^2 \text{ yr} \quad (34)$$

where we have used $\phi_{\text{sp}} = 1 \%$ and $N_{\text{cl}} = 2 \times 10^3$.

Lazarian & Efroimsky (1999) argued that the deformation induces important energy dissipation. The timescale of inelastic dissipation is

$$t_{\text{ine}} \approx 2^{11} 3^{-2.5} g(s) a_{\text{eff}}^{11/2} \left(\frac{J}{J_T} \right)^{-3/2} (k_B T_g)^{-3/2} \mu Q \rho_s^{1/2} \quad (35)$$

$$g(s) = \frac{s^{-1/3} [1 + s^2]^4}{64 s^4 + 20} \quad (36)$$

where Q is the inelastic parameter, and μ is rigid module. For a silicate grain with axis ratio 1:2 ($s = 0.5$), we obtain

$$t_{\text{ine}} \approx 8.7 a_{-5}^{11/2} \left(\frac{J}{J_T} \right)^{-3/2} \hat{T}_d^{-3/2} \hat{\mu} \hat{Q} \hat{\rho}_s^{1/2} \text{ yr} \quad (37)$$

where $\hat{Q} = Q/100$, $\hat{\mu} = \mu/10 \text{ Pa}$.

Internal alignment is caused by the complex of energy dissipation processes described above; then the internal alignment timescale is

$$\frac{1}{t_{\text{int}}} \approx \frac{1}{t_{\text{Bar}}} + \frac{1}{t_{\text{nuc}}} + \frac{1}{t_{\text{sup}}} + \frac{1}{t_{\text{ine}}} \quad (38)$$

Figure 2 shows the internal relaxation timescale as a function of the grain radius. In the presence of superparamagnetic inclusions, internal relaxation is dominated by superparamagnetic Barnett relaxation for smaller grains and by nuclear relaxation for larger grains. Since $t_{\text{nuc}} \propto a_{\text{eff}}^7$, internal relaxation does not likely to occur for larger grains, e.g., mm-size grains for which the timescale is longer than the age of the universe.

2.3. Conditions for the alignment

CL07 assumed alignment happens when the energy density of the radiation field is large enough to spin up grains to a suprathermal state according to Draine & Weingartner (1996). However, as we mentioned in Section 2.1, the

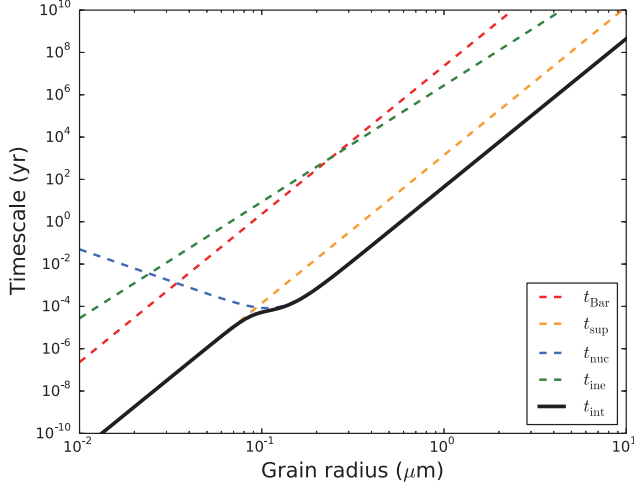


Figure 2. Timescale of internal alignment. Adopted parameters are $s = 0.5$, $J = J_T$, $f_p = 0.1$, $\phi_{sp} = 0.01$, and $N_{cl} = 2 \times 10^3$.

suprathernal rotation is not always necessary for grain alignment. In addition, CL07 assumed the alignment axis is always parallel to the local magnetic field, but this is not true because grains can be aligned with the radiation direction (LH07). Here, we state the alignment condition adopted in this paper.

2.3.1. Alignment axis

The precession motion of a grain is essential for grain alignment because the precession axis will be the alignment axis. Denoting the timescale of precession t_p , which is adopted as a minimum value of the Larmor precession, t_L (Equation 7) or the radiative precession, $t_{rad,p}$ (Equation 18), we have

$$t_p = \min(t_{rad,p}, t_L) \quad (39)$$

The grain alignment occurs when $t_p < t_{gas}$, where t_{gas} is the gaseous damping timescale. If $t_{gas} < t_p$, the precession motion of a grain is suppressed, hence no alignment is possible. As shown by LH07, when Larmor precession dominates radiative precession, or $t_{rad,p}/t_L > 1$, the grain angular momentum vector \mathbf{J} is aligned with respect to the direction of the local magnetic field \mathbf{B} ($\xi \rightarrow 0$ in Figure 1). When radiative precession dominates Larmor precession, or $t_{rad,p}/t_L < 1$, the grain angular momentum vector \mathbf{J} is aligned with the direction of the anisotropic radiation \mathbf{k} ($\Theta \rightarrow 0$ in Figure 1).

The timescale of fast alignment⁷ to \mathbf{B} or \mathbf{k} due to RAT is somewhat longer than the precessions timescale (see Figure 29 in LH07), and

$$t_{rad, align} \approx C t_p \quad (40)$$

where $C = 30 \sim 100$. In this work, we adopt $C = 30$. Equation (40) expresses the timescale of grain alignment with respect to both the magnetic field and the radiative flux.

2.3.2. Degree of alignment

From a statistical point of view, grain alignment means that the distribution of an alignment angle η , which is the angle between the grain axis \hat{a}_1 and the precession axis (the magnetic field vector \hat{B} or the anisotropic radiation \hat{k}), should be

⁷ LH07 regarded fast alignment as an analogy of a fast dynamo, since RAT alignment can take place faster than the gaseous damping timescale.

$\langle \cos^2 \eta \rangle < 1/3$ where the brackets denote the average over the ensemble of dust grains. For randomly orientated grains, $\langle \cos^2 \eta \rangle = 1/3$. We define the degree of RAT alignment by $Q_{RATs} = (3\langle \cos^2 \eta \rangle - 1)/2$. In the same way, we define the degree of internal alignment by $Q_{int} = (3\langle \cos^2 \theta \rangle - 1)/2$.

We write the degree of grain alignment $\mathcal{R}(a)$ of distribution of dust grains approximately as

$$\mathcal{R}(a) \approx f_{high-J} Q_{RATs}^{high-J} Q_{int}^{high-J} + (1 - f_{high-J}) Q_{RATs}^{low-J} Q_{int}^{low-J} \quad (41)$$

where f_{high-J} is the fraction of grains in high- J attractors. f_{high-J} depends on the grain size, shape, and optical properties. Since the properties of dust aggregates in protoplanetary disks are poorly understood, we treat f_{high-J} as a free parameter throughout this paper. Hence, $f_{high-J} = 1$ corresponds to the case for grains to be aligned most efficiently (the optimistic case), while $f_{high-J} = 0$ is the most difficult condition for grains to be aligned (the pessimistic case).

At high- J attractors, the degree of RAT alignment does not depend on internal relaxation (LH07; Hoang & Lazarian 2009b); hence we can approximately write

$$Q_{RATs}^{high-J} = \begin{cases} 1, & (t_{rad,align} < t_{gas}) \\ 0, & (t_{rad,align} \geq t_{gas}). \end{cases} \quad (42)$$

On the other hand, at low- J attractors, the degree of RAT alignment does depend on internal alignment (Hoang & Lazarian 2009a). Then, we adopt

$$Q_{RATs}^{low-J} = \begin{cases} 0.2, & (t_{int} < t_{rad,align} < t_{gas}) \\ 0.1, & (t_{rad,align} < t_{int} < t_{gas}) \\ 0.1, & (t_{rad,align} < t_{gas} < t_{int}) \\ 0, & (t_{rad,align} \geq t_{gas}), \end{cases} \quad (43)$$

Since perfect internal alignment minimizes their rotational kinetic energy, suprathernally rotating grains readily become internally aligned through transferring their rotational kinetic energy into vibrational energy (e.g., Draine 2011). In addition, grains in a state of high- J attractors are not likely to change their angular momentum vector by gas collisions because each of gas particle deposits only a small amount of angular momentum compared to the grain angular momentum. Hence, the degree of internal alignment at high- J attractors is always expected to be almost perfect; then we set $Q_{int}^{high-J} = 1$. On the other hand, at low- J attractors, the rotational kinetic energy can be affected by its own thermal fluctuation and also gas bombardment. Therefore, in this case, the degree of internal alignment should not be 100%. In the absence of internal alignment, low- J attractors behave in two different ways: some attractors are aligned parallel to \mathbf{J} (“right” alignment), while the others are aligned perpendicular to \mathbf{J} (“wrong” alignment) (Hoang & Lazarian 2008). We assume $Q_{int}^{low-J} = 0.5$. A more detailed calculation of Q_{int} for dust aggregates in the absence of internal relaxation is necessary, but this is beyond the scope of this study. Table 1 shows the degree of alignment $\mathcal{R}(a)$ calculated with Equation (41).

3. DISK AND DUST MODELS

3.1. The disk model and method

Table 1
Model of degree of alignment, $\mathcal{R}(a)$, defined by Equation (41)

timescales	$f_{\text{high-}J} = 1$	$f_{\text{high-}J} = 0.5$	$f_{\text{high-}J} = 0$
$t_{\text{gas}} < t_p$	0 %	0 %	0 %
$t_{\text{int}} < t_{\text{rad,align}} < t_{\text{gas}}$	100 %	55 %	10 %
$t_{\text{rad,align}} < t_{\text{int}} < t_{\text{gas}}$	100 %	52.5 %	5 %
$t_{\text{rad,align}} < t_{\text{gas}} < t_{\text{int}}$	100 %	50 %	0 %

The surface density profile of dust grains in the disk is assumed to be a similarity solution, given by

$$\Sigma_d = (2 - \zeta) \frac{M_d}{2\pi R_c^2} \left(\frac{R}{R_c} \right)^{-\zeta} \exp \left[- \left(\frac{R}{R_c} \right)^{2-\zeta} \right] \quad (44)$$

where M_d is the disk dust mass, R_c is the cut-off radius, and R is the disk radius (Lynden-Bell & Pringle 1974). For simplicity, the vertical distribution of dust grains is assumed to be Gaussian, $\rho_d = \Sigma_d / (\sqrt{2\pi} H_d) \exp[-(z^2/2H_d^2)]$, where H_d is the dust scale height. The parameters adopted in this study are as follows: $M_d = 10^{-4} M_\odot$, $\zeta = 1.0$, $R_{\text{in}} = 0.1$ au, $R_{\text{out}} = 100$ au, $R_c = 20$ au, $H_d = 3.3 \times 10^{-2} (R/1 \text{ au})^{1.25}$ au. The central star is assumed to be a T-Tauri star with a mass of $0.5 M_\odot$, the effective temperature of 4000 K, and the radius of $2 R_\odot$. Note that although the mass of the star does not come into the radiative transfer calculations, it is used in the dust density calculation through the Kepler frequency in Section 5.2.

Based on the star and disk model, we perform a radiative transfer calculation to determine the dust temperature at each location of the disk. The radiative transfer calculation is performed with the 3D Monte Carlo radiative transfer code, RADMC-3D⁸. The number of grids is $N_r = 256$ for $R_{\text{in}} < R < R_{\text{out}}$, $N_\phi = 256$ for $0 < \phi < 2\pi$, and $N_\theta = 128$ for $\pi/3 < \theta < 2\pi/3$ (Figure 3). The number of photons is set as 10^9 .

In the radiative transfer calculation, dust grains are assumed to be spherical, and this allows us to use an exact solution for the optical properties from the Mie theory (e.g., Bohren & Huffman 1983). In addition, we average over the optical properties with respect to the power-law size distribution,

$$n(a)da \propto a^p da \quad (a_{\text{min}} < a < a_{\text{max}}) \quad (45)$$

where $n(a)da$ is the number of spherical dust grains having sizes of a to $a + da$. We assume the grains are well mixed in the gas density distribution. We adopt the following parameters for the grain size distribution: $a_{\text{min}} = 0.005 \mu\text{m}$, $a_{\text{max}} = 100 \mu\text{m}$, $p = -3.5$. The dielectric function of the grains is assumed to be a mixture of the silicate and the H_2O ice (Miyake & Nakagawa 1993).

Based on the temperature structure determined by RADMC-3D, the energy density of radiation field at each location is calculated by

$$u_{\text{rad},\nu}(r, \theta) = \frac{1}{c} \left\{ \int_0^{2\pi} I_\nu(\alpha) d\alpha + B_\nu(T_*) \Delta\Omega_* e^{-\tau_{\nu,*}} \right\} \quad (46)$$

where $\Delta\Omega_* = \pi(R_*/r)^2$ denotes the solid angle of the star, r is the distance from the star, and $\tau_{\nu,*}$ is the optical depth along the line of sight of the central star. The intensity at the i th grid, $I_\nu^i(\alpha)$, is calculated by solving

$$I_\nu^i(\alpha) = B_\nu(T_d^i)(1 - e^{-\delta\tau_i}) + \sum_{j \neq i} B_\nu(T_d^j)(1 - e^{-\Delta\tau_j})e^{-\tau_{ij}} \quad (47)$$

⁸ The code and more information are available on <http://www.ita.uni-heidelberg.de/~dullemond/software/radmc-3d/>

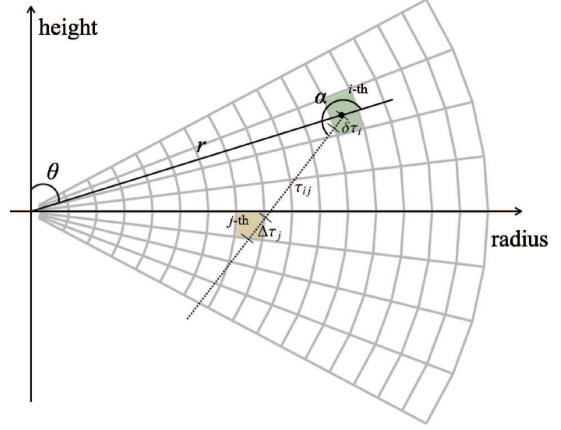


Figure 3. Schematic illustration of integration of intensity along the line of sight. We use spherical coordinates with a $N_r = 256$, $N_\theta = 128$ mesh.

where T_d^j is the dust temperature on the j th grid, $\delta\tau_i$ is the optical depth from the i th grid center to the i th grid wall, τ_{ij} is the optical depth of the i th and the j th grid wall, and $\Delta\tau_j$ is the optical depth of the j th grid. The summation is performed along the line of sight. We neglect the scattered starlight because at the surface layer RAT is dominated by the direct emission from the star.⁹ The anisotropy parameter γ_ν is calculated approximately by

$$\gamma_\nu \approx \frac{I_\nu(\alpha = 180^\circ) - I_\nu(\alpha = 0^\circ)}{I_\nu(\alpha = 180^\circ) + I_\nu(\alpha = 0^\circ)} \quad (48)$$

3.2. A magnetic field strength and topology

The magnetic field strength is one of the most uncertain quantities in protoplanetary disks. Global magnetohydrodynamics (MHD) simulation of disks suggests that the magnetic field is dominated by the toroidal component because of the disk shear flow (e.g., Flock et al. 2015). Hence, we only consider the toroidal magnetic field. Okuzumi et al. (2014) studied the radial transport of the magnetic field and estimated an upper limit on the vertical field strength. They found that the maximum vertical field strength is

$$B_{z, \text{max}}(R) = 1 \text{ mG} \left(\frac{R}{10 \text{ au}} \right)^{-2}. \quad (49)$$

The toroidal magnetic field can be amplified up to 10 times larger than the initial vertical magnetic field strength. However, $B_{z, \text{max}}(R)$ indicates the maximum value of the initial vertical B -field strength, and the actual strength may be smaller; hence, we assume $B_{z, \text{max}}(R)$ as the toroidal B -field strength.

4. GRAIN ALIGNMENT IN THE DISK

4.1. Anisotropic radiation field in the disk

In Figure 4, we show the energy density of the radiation field, the spectrum weighted wavelength, and the anisotropy parameter in the disk. Above the disk photosphere, the energy density of radiation is dominated by the stellar radiation. Hence, at the surface layer, $u_{\text{rad}} \approx \mathcal{A}T^4 \Delta\Omega_*$, where

⁹ If dust grains at the surface layer have a large albedo, scattered starlight may dominate the disk mid-infrared polarization, and polarized thermal emission arising from aligned grains becomes subdominant. In this case, we expect an azimuthal polarized vector for face-on disks. Note that even in this case, we expect circular polarization from the disk as discussed in Section 6.3

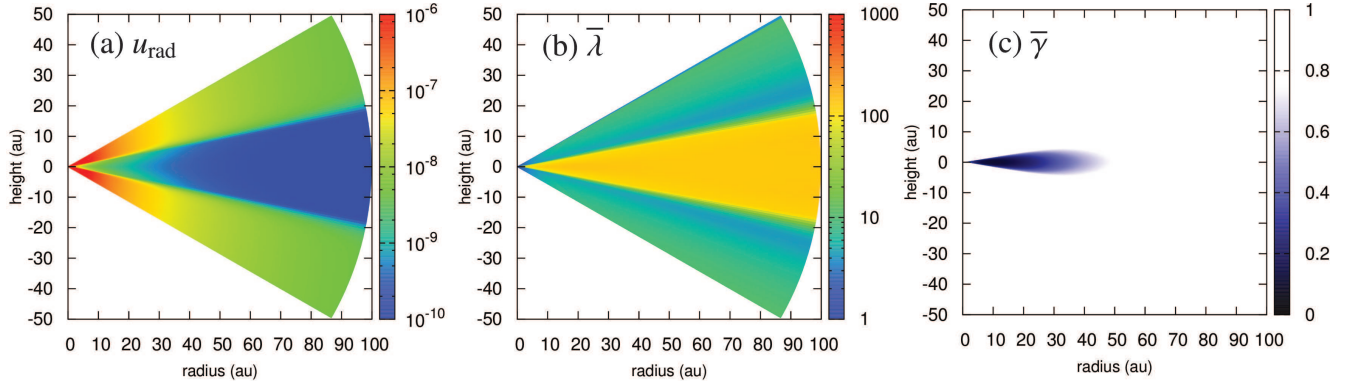


Figure 4. The radiation field in the disk. (a) Energy density of the radiation u_{rad} [erg cm^{-3}] (b) the spectrum averaged wavelength $\bar{\lambda}$ [μm], and (c) the spectrum averaged anisotropy parameter $\bar{\gamma}$ are shown.

$\mathcal{A} = 7.57 \times 10^{-15} \text{ erg cm}^{-3} \text{ K}^{-4}$ is the radiation constant, and then

$$u_{\text{rad}} \approx 5.2 \times 10^{-6} \text{ erg cm}^{-3} \left(\frac{R}{10 \text{ au}} \right)^{-2} \quad (50)$$

for $T_* = 4000 \text{ K}$ and $R_* = 2R_\odot$. The anisotropy parameter of the radiation field is almost unity, and \mathbf{k} is pointing radially outward.

At the disk midplane, the energy density of the radiation is 2 – 3 orders of magnitude lower than that at the surface layer because the disk is optically thick at visible/NIR wavelengths. The energy density of the radiation field at the midplane is dominated by the thermal emission from cold grains at the midplane ($\bar{\lambda} \approx 140 \mu\text{m}$). Even in the midplane, the radiation energy density is still very large compared to the interstellar radiation field, $u_{\text{ISRF}} = 8.64 \times 10^{-13} \text{ erg cm}^{-3}$ (Mathis et al. 1983). As shown in Figure 4(c), the anisotropy parameter becomes around 0.1 at the midplane at $R \lesssim 30 \text{ AU}$ because the disk becomes optically thick for the radiation with $\bar{\lambda} \approx 140 \mu\text{m}$. Therefore, in this region, only 10 % of the energy density can contribute the RAT because only the anisotropic radiation field is important for RAT alignment. At the outer region, the disk becomes optically thin, and the radiation anisotropy is almost 100 % and it coincides with the radial direction. It is worth noting that when we consider a dust ring structure with an inner hole around the central star, the radiation anisotropy can be in the azimuthal direction (Kataoka et al. 2015). Dust grains may become aligned with the azimuthal radiative flux if the ring is not uniform along the azimuthal direction. In this paper, we assume a smooth disk density distribution from the region near the central star to the outer disk; thereby, the anisotropic radiation directs radially outward.

4.2. RAT alignment timescale in the disk

Based on the radiation field calculated in Section 4.1, we calculate the characteristic timescales relevant to grain alignment in the disk. Figure 5 shows the timescales relevant to RAT alignment at two different locations (midplane and surface at $R = 50 \text{ au}$) in the disk.

The alignment timescale shown in the top panels in Figure 5 indicates the minimum size of dust grains to be aligned. In general, smaller grains experience stronger gaseous damping and also the RAT becomes less efficient; therefore, only large grains can be aligned. A critical grain size is given by the balance between the RAT alignment timescale ($t_{\text{rad, align}}$) and the

gaseous damping timescale (t_{gas}). At the midplane of $R = 50 \text{ au}$, the RAT is determined by the radiation field emitted from ambient thermal grains with $\bar{\lambda} \approx 140 \mu\text{m}$, and then for smaller grains, $a \leq 140 \mu\text{m}/1.8 \approx 80 \mu\text{m}$, the RAT becomes less efficient (see Equation 17). Figure 5 shows that at the midplane of $R = 50 \text{ au}$, the critical grain size is $\approx 27 \mu\text{m}$. As a result, external alignment for a mm-sized grain is possible even at the dense midplane, although these grains may not show internal alignment (see Figure 2). At the surface layer, the gas density is much lower than the that at the midplane, and the radiation field has a shorter wavelength than the midplane; hence, external alignment of smaller grains is possible. Figure 5 shows the critical grain size at the disk surface is $\approx 0.2 \mu\text{m}$.

The bottom panels in Figure 5 show the precession timescales of dust grains, and these define the alignment axis. As we mentioned in Section 2, the alignment axis is determined by the dominant precession motion of the grains. Figure 5 shows that, at the midplane, a dust grain which is larger than the critical size precesses around the radiative flux; therefore, these grains become aligned with radiation direction. Even if we consider superparamagnetic inclusions, Larmor precession is still slow compared to radiative precession. Therefore, these grains become aligned with respect to the radiation direction, not to the magnetic field. Note that the direction of radiation at the midplane of $R = 50 \text{ au}$ is radially outward; hence, the aligned grains are expected to produce azimuthally polarized emission. In addition to the fast radiative precession, it is also found that Larmor precession is often suppressed by the gaseous damping. The presence of superparamagnetic inclusions enhances the magnetic susceptibility significantly; nevertheless, only grains smaller than $\approx 10 \mu\text{m}$ can overcome the gaseous damping. This result also illustrates the difficulty of grain alignment with respect to the magnetic field in the disk midplane. A critical grain size for which the Larmor precession timescale equals to the gaseous damping can be obtained from Equations (3) and (7):

$$a_{\text{crit}} \approx 0.1 \mu\text{m} \hat{\rho}_g^{-1} \hat{T}_g^{-1/2} \hat{\chi} \left(\frac{B}{1 \text{ mG}} \right). \quad (51)$$

If the grain size is larger than this critical size, Larmor precession is suppressed by the gaseous damping. In summary, (sub-)mm-sized dust grains at the midplane are difficult to align with the magnetic field due to the efficient gaseous damping as well as fast radiative precession; however, these grains may align with the radiation direction.

At the surface layer, a grain size larger than $0.2 \mu\text{m}$ can be

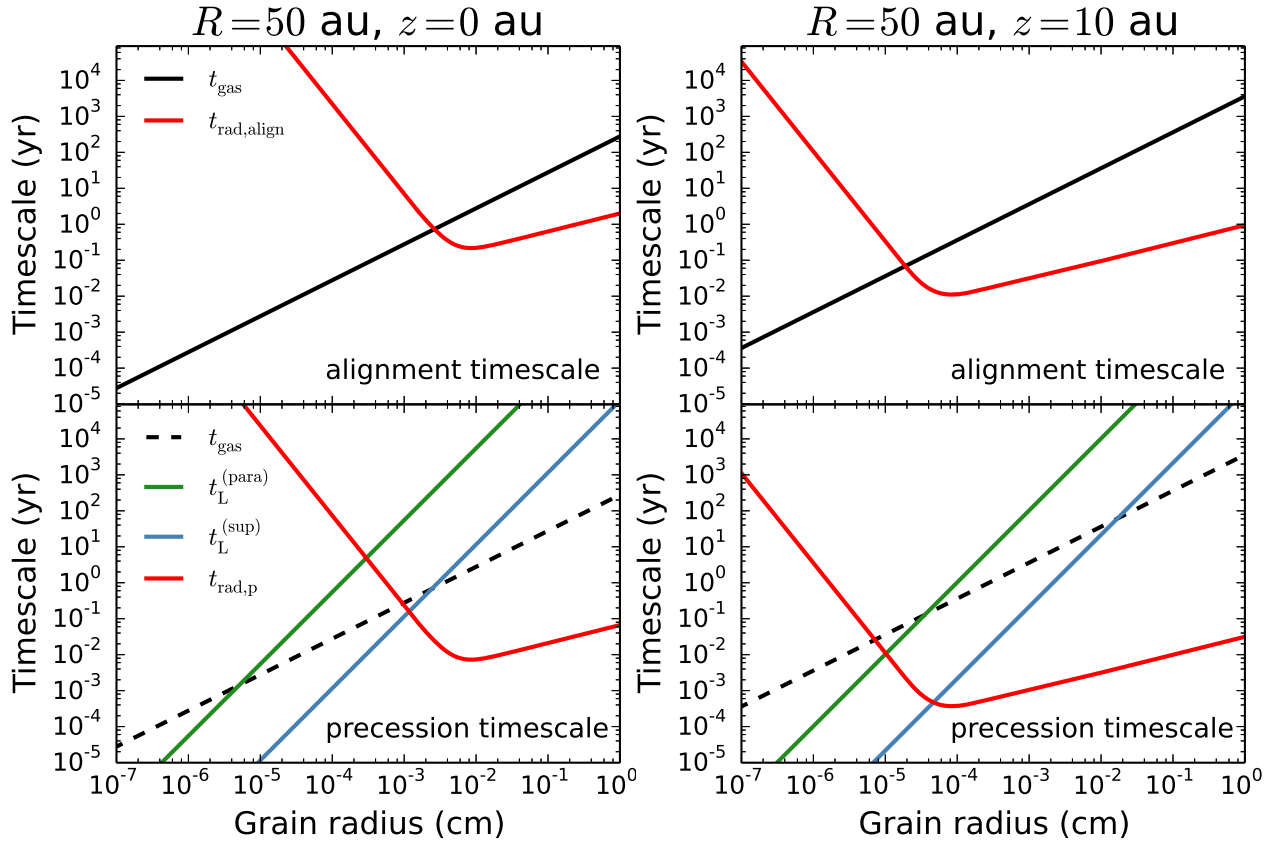


Figure 5. Timescales relevant to RAT alignment. Top and bottom panels show the alignment timescales and the precession timescales, respectively. Left and right panels correspond to the two different locations in the disk, $(R, z) = (50 \text{ au}, 0 \text{ au})$, and $(R, z) = (50 \text{ au}, 10 \text{ au})$, respectively. For the top panels, black and red lines represent the timescale of the gaseous damping (t_{gas}) and the RAT alignment timescale ($t_{\text{rad, align}}$). For the bottom panels, the red solid line indicates the radiative precession timescale ($t_{\text{rad, p}}$). Green and blue lines show the Larmor precession timescale (t_L) for paramagnetic inclusions ($f_p = 10\%$) and superparamagnetic inclusions ($f_p = 10\%$, $\phi_{\text{sp}} = 3\%$, $N_{\text{cl}} = 2 \times 10^3$), respectively. The dashed line in the bottom panels represents the gaseous damping timescale.

aligned. Figure 5 shows that sub-micron-sized grains can be aligned with the magnetic field, while larger grains become aligned with the radiation direction. These grains may contribute to the mid-infrared polarization of the disk because the disk is optically thick at mid-infrared wavelength, and then the surface grains are responsible for the polarized flux. Although sub-micron-sized grains without superparamagnetic inclusions align with the radiation direction at surface layer, those with superparamagnetic inclusions can become aligned with the magnetic field. As a result, in mid-infrared polarimetry, we expect magnetic field alignment for grains having superparamagnetic inclusions.

Finally, it is worth mentioning how carbonaceous grains affect on grain alignment. As shown in LH07, the alignment induced with respect to the radiation direction is mostly independent of the grain composition, while the alignment with respect to the magnetic field depends on the Larmor precession frequency, which is significantly reduced for carbonaceous grains. As a result, the introduction of the carbonaceous grains results in increasing the radius over which the grains are aligned with respect to the radiation direction.

5. DEGREE OF POLARIZATION OF THE DISK

We calculate the polarization flux arising from aligned grains, and estimate the degree of polarization of the disk. To focus on how grain alignment affects on the degree of polarization, we neglect the polarization due to the scattering. In addition, we assume a face-on disk for the sake of simplicity;

the effect of disk inclination is discussed in Section 6.2. In Section 5.1, we describe an analytical model of the degree of linear polarization arising from a single ellipsoid. In Section 5.2, we present a model of the disk polarization with/without dust settling. The results are presented in Section 5.3, 5.4, and 5.5.

5.1. Linear degree of polarization of an ellipsoid

CL07 calculated the absorption cross section along the minor axis and the major axes using the DDSCAT code (Draine & Flatau 1994); the degree of polarization is obtained by

$$p = \frac{C_{\text{abs}, \perp} - C_{\text{abs}, \parallel}}{C_{\text{abs}, \perp} + C_{\text{abs}, \parallel}} \quad (52)$$

where $C_{\text{abs}, \perp}$ and $C_{\text{abs}, \parallel}$ are the absorption cross section for $\mathbf{E} \perp \hat{\mathbf{a}}_1$ and $\mathbf{E} \parallel \hat{\mathbf{a}}_1$, respectively, where \mathbf{E} represents the electric field vector of the light. Obviously, for a spherical grain, $C_{\text{abs}, \perp} = C_{\text{abs}, \parallel}$; therefore, unpolarized thermal emission is radiated. CL07 showed that the degree of polarization becomes almost zero when a grain radius is larger than $\lambda/2\pi$, e.g., the geometrical optics limit. Hence, we assume

$$p(a_{\text{eff}}, \lambda) \approx \begin{cases} \frac{C_{\text{abs}, \perp} - C_{\text{abs}, \parallel}}{C_{\text{abs}, \perp} + C_{\text{abs}, \parallel}}, & 2\pi a_{\text{eff}} < \lambda \\ 0, & \text{otherwise.} \end{cases} \quad (53)$$

For $2\pi a_{\text{eff}} < \lambda$, we use an electrostatic analysis of the ellipsoid (Rayleigh approximation) to find the value of $C_{\text{abs}, \perp}$ and

$C_{\text{abs},\parallel}$ (e.g., [Bohren & Huffman 1983](#)). Suppose α_j is the polarizability of the ellipsoid with respect to the axis j , where j runs from 1 to 3; then it becomes

$$\alpha_j = 4\pi a_1 a_2^2 \frac{m^2 - 1}{3 + 3L_j(m^2 - 1)}, \quad (54)$$

where L_j is a geometrical parameter and m is the complex refractive index. In the case of an oblate ellipsoid, the geometrical parameter satisfies $L_1 = L_2 < L_3$ and $L_1 + L_2 + L_3 = 1$. In this case, L_1 becomes

$$L_1 = \frac{g(e)}{2e^2} \left[\frac{\pi}{2} - \arctan(g(e)) \right] - \frac{g(e)^2}{2} \quad (55)$$

$$g(e) = \left(\frac{1 - e^2}{e^2} \right)^{1/2} \quad (56)$$

where $e^2 = 1 - s^2$. The absorption cross section is given by the optical theorem, $C_{\text{abs}} = k \text{Im}(\alpha_j)$, where k is a wavenumber. Denoting the complex refractive index by $m = n + ik$ ¹⁰, and assuming a less absorbing grain ($k \ll 1$), we obtain

$$C_{\text{abs},j} \simeq \frac{2\pi}{\lambda} V \frac{2nk}{[L_j(n^2 - 1) + 1]^2} \quad (57)$$

where V is the volume of an ellipsoid. Finally, we obtain

$$\frac{C_{\text{abs},\perp}}{C_{\text{abs},\parallel}} = \frac{[L_3(n^2 - 1) + 1]^2}{[L_1(n^2 - 1) + 1]^2} \quad (58)$$

where $L_3 = 1 - 2L_1$. Since the geometrical parameter L depends only on the axis ratio of the grains, Equation (58) is irrelevant to the grain size a_{eff} . In Figure 6, we plot Equation (52) for a Rayleigh approximation. When we assume astronomical silicate ([Draine & Lee 1984](#); [Laor & Draine 1993](#)) as the dielectric function, and adopt $\lambda = 850\mu\text{m}$, Equation (52) gives $C_{\text{abs},\perp}/C_{\text{abs},\parallel} = 1.6$ for $s = 0.77$, and hence the degree of polarization is 22%. For $s = 0.67$, the ratio is

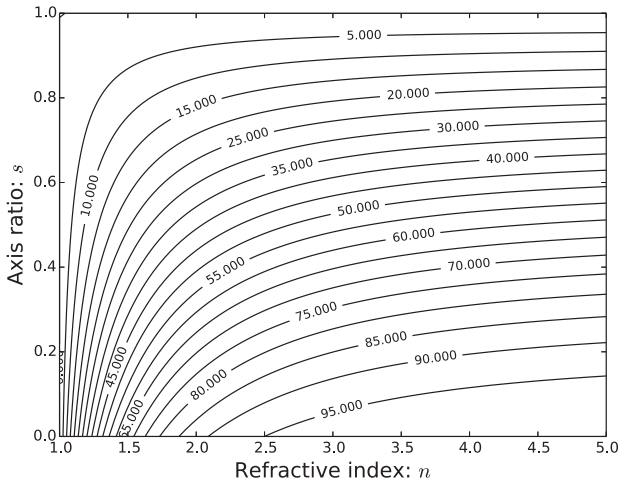


Figure 6. Degree of polarization arising from an oblate spheroid with an axis ratio of s and a refractive index of n in the Rayleigh limit, calculated using Equations (58) and (52).

¹⁰ The symbol k is used to denote the wavenumber, while the imaginary part of the complex refractive index is denoted by k according to [Bohren & Huffman \(1983\)](#).

$C_{\text{abs},\perp}/C_{\text{abs},\parallel} = 2.1$, and hence, the degree of polarization is 35%. These results are compatible with the DDA calculations of [CL07](#).

5.2. Polarized emission from the disk

Combining with the temperature structure obtained by using RADMC-3D and the degree of polarization of a single oblate grain (Equation 52), we can calculate the polarized flux from the disk.

The disk model we presented in Section 3 assumed a well-mixed population of dust grains with the gas at everywhere in the disk. In other words, the grain size distribution is the same in every grid cell in the disk. However, this assumption may lead to an underestimation of the degree of polarization at mid-infrared wavelengths. This is because the presence of dust grains larger than the observing wavelength at the surface layer reduces the polarization degree (Equation 53), while such large grains are expected to be depleted from the surface layer due to dust settling. Hence, we consider dust settling in the calculation of the polarized emission in order to study its effect on the results. To reduce the computational cost, we adopt the following assumptions in the ray-tracing procedure. Firstly, the temperature of each grid cell in the disk is assumed to be the same as in Section 3. Secondly, we calculate the emissivity on each grid cell taking dust settling into account (see Section 5.2.1 for more details). Thirdly, for a given emissivity of each grid cell, the ray-tracing calculation is performed.

5.2.1. Spatial and size distribution model of grains

We assume the grain surface number density in a size range $[a, a + da]$, $\mathcal{N}(R, a)$, obeys a power-law with power-law index -3.5 ; then

$$\mathcal{N}(R, a)da = \mathcal{N}_0(R)a^{-3.5}da \quad (a_{\min} < a < a_{\max}) \quad (59)$$

Since

$$\Sigma_d(R) = \int_{a_{\min}}^{a_{\max}} \frac{4}{3}\pi a^3 \rho_s \mathcal{N}(R, a)da, \quad (60)$$

we obtain the radial distribution of the grain surface number density,

$$\mathcal{N}_0(R) = \frac{3}{8\pi \rho_s} \frac{\Sigma_d}{[a_{\max}^{1/2} - a_{\min}^{1/2}]^{-1}} \quad (61)$$

We simply assume a Gaussian density profile in the vertical direction; then the dust density in a size range $[a, a + da]$ can be written by

$$\rho_d(R, z, a)da = \rho_d(R, 0, a) \exp\left[-\frac{z^2}{2h_d^2}\right]da \quad (62)$$

where h_d is the dust scale height. Assuming that this is determined by the balance between gravitational settling and turbulent diffusion ([Youdin & Lithwick 2007](#)), we have

$$h_d = h_g \left(1 + \frac{\Omega t_s}{\alpha} \frac{1 + 2\Omega t_s}{1 + \Omega t_s} \right)^{-1/2} \quad (63)$$

where Ω is the Kepler angular velocity, α is the turbulent strength, h_g is the gas pressure scale height, and t_s is the stopping time given by

$$t_s = \begin{cases} t_s^{(\text{Ep})} \equiv \frac{3m}{4\rho_s v_{\text{th}} A}, & a < \frac{9}{4}\lambda_{\text{mfp}}, \\ t_s^{(\text{St})} \equiv \frac{4a}{9\lambda_{\text{mfp}}} t_s^{(\text{Ep})}, & a > \frac{9}{4}\lambda_{\text{mfp}}, \end{cases} \quad (64)$$

where (Ep) and (St) indicate the Epstein and Stokes drag laws, respectively, m is the mass of the grain, A is the cross section of the grain, and $\lambda_{\text{mfp}} = \mu m_{\text{H}} / \sigma_{\text{mol}} \rho_g$ is the mean free path of a gas molecule, where we adopt $\sigma_{\text{mol}} = 2 \times 10^{-15} \text{ cm}^2$ as the collisional cross section of a molecule. By integrating Equation (62) with respect to z , we can obtain

$$\rho_d(R, 0, a) = \frac{1}{2} \frac{\Sigma_d}{\sqrt{2\pi} h_d} \left[a_{\text{max}}^{1/2} - a_{\text{min}}^{1/2} \right]^{-1} a^{-\frac{1}{2}} \quad (65)$$

As a result, the number density of dust grains in the size range $[a, a + da]$ is

$$n(R, z, a) da = \frac{3\rho_d(R, z, a)}{4\pi a^3 \rho_s} da \quad (66)$$

$$= \frac{3}{8\pi} \frac{\Sigma_d / \rho_s}{\sqrt{2\pi} h_d} \left[a_{\text{max}}^{1/2} - a_{\text{min}}^{1/2} \right]^{-1} a^{-3.5} \exp \left[-\frac{z^2}{2h_d^2} \right] da \quad (67)$$

5.2.2. Polarization degree of emission of grains with size distribution

To calculate the emissivity, we define a locally averaged grain opacity, $\langle \kappa_{\text{abs}, \text{sca}} \rangle(R, z)$ by

$$\langle \kappa_{\text{abs}} \rangle(R, z) = \frac{\int_{a_{\text{min}}}^{a_{\text{max}}} n(R, z, a) a^3 \kappa_{\text{abs}}(a) da}{\int_{a_{\text{min}}}^{a_{\text{max}}} n(R, z, a) a^3 da} \quad (68)$$

At each location in the disk, the intrinsic degree of polarization is

$$\langle p_0(R, z, \lambda) \rangle = \frac{\int_{a_{\text{min}}}^{a_{\text{max}}} (-1)^n P(a, \lambda) \mathcal{R}(a) \kappa_{\text{abs}}(a, \lambda) a^3 n(R, z, a) da}{\int_{a_{\text{min}}}^{a_{\text{max}}} \kappa_{\text{abs}}(a, \lambda) a^3 n(R, z, a) da} \quad (69)$$

where we insert $(-1)^n$ so that the direction of polarization is considered. We assume that the polarization degree becomes negative ($n = 1$) for a radial \mathbf{E} -vector ($t_L / t_{\text{rad}, p} < 1$) and positive ($n = 2$) for an azimuthal \mathbf{E} -vector ($t_L / t_{\text{rad}, p} > 1$). n and $\mathcal{R}(a)$ are calculated with the radiation field given in Figure 4. The absorption opacity in Equation (69) is calculated by using the Mie theory, regarding an oblate as a sphere with a_{eff} .

Plugging Equation (53) into Equation (69), we obtain

$$\langle p_0(R, z, \lambda) \rangle = \frac{C_{\text{abs}, \perp} - C_{\text{abs}, \parallel}}{C_{\text{abs}, \perp} + C_{\text{abs}, \parallel}} \times \frac{\int_{a_{\text{min}}}^{a_{\text{large}}} (-1)^n \mathcal{R}(a) \kappa_{\text{abs}}(a, \lambda) a^3 n(R, z, a) da}{\int_{a_{\text{min}}}^{a_{\text{max}}} \kappa_{\text{abs}}(a, \lambda) a^3 n(R, z, a) da} \quad (70)$$

where $a_{\text{large}} \equiv \min(a_{\text{max}}, \lambda / 2\pi)$ represents the maximum size of dust grains being aligned. In Equation (70), we assume for simplicity that a_2 / a_1 is constant through the grain size distribution and all grains have the same temperature.

Using Equations (68) and (70), we calculate the polarized intensity and the total intensity via the ray-tracing method (Figure 3). The polarization degree is then obtained as the polarized intensity divided by the intensity at each radius of the disk.

5.3. Alignment of grains without magnetic inclusions

In Figure 7, we plot a map of the degree of polarization of the disk with a polarization vector at mid-infrared wavelength

($\lambda = 12 \mu\text{m}$) and millimeter wavelength ($\lambda = 870 \mu\text{m}$). The dust grains are assumed to be magnetically poor ($f_p = 0.01$ and $\phi_{\text{sp}} = 0$) and the disk magnetic field model is given in Section 3.2. Figure 7 shows that for both mid-infrared and submillimeter wavelengths, the polarization vector shows a centrosymmetric pattern. This is because the dust grains align with the radiation direction (see also Figure 5). Therefore, even in the presence of a toroidal magnetic field, the polarization vector can be in the azimuthal direction for both mid-infrared wavelength and millimeter wavelengths.

The radial dependence of the degree of polarization differs depending on dust settling, or the turbulent strength, as shown in Figure 8. For the case of no dust settling, the radial dependence is not strong for both of mid-infrared and millimeter wavelengths.

At mid-infrared wavelength with $\alpha = 10^{-1}$ and 10^{-2} , the degree of polarization increases with increasing the disk radius, and at the inner region, it coincides with that of the no-settling case. This is because at the inner region, the gas density is sufficiently high that the largest grains can be well coupled to the gas. On the other hand, at the outer region, the largest grains settle down to the midplane because of the low gas density. Since grains larger than the observing wavelength reduce the degree of polarization, their depletion from the surface layer can enhance the mid-infrared polarization degree. If we consider a disk with weak turbulence, $\alpha = 10^{-3}$, the degree of polarization of the outer disk decreases with increasing the disk radius. Under very weak turbulence, micron-sized grains also settle down, and only sub-micron-sized grains can be stirred up to the surface layer. However, sub-micron-sized metal poor grains do not show external alignment, as shown in Figure 5. As a result, dust settling leads to a reduction of the polarization degree. Note that once micron-size dust grains settle down to the midplane, they hardly contribute to mid-infrared polarization because the gas density at the midplane is high, so that the gaseous damping timescale is short, and the wavelength of the radiation field is long, and so RAT is inefficient for such grains. Therefore, these grains are not likely to be aligned.

Li et al. (2016) concluded that the gradual increase of polarization degree is due to the scattering. Our result shows that in the presence of dust settling with a moderate strength of turbulence may also produce a monotonically increasing radial dependence of the degree of polarization.

At the millimeter wavelength region, the radial dependence does not change significantly except for the case of $\alpha = 10^{-3}$. For a low-turbulent disk ($\alpha = 10^{-3}$), efficient dust settling results in the formation of a thin layer of large particles at the midplane, i.e., $a \geq \lambda / 2\pi \approx 140 \mu\text{m}$; hence, at the region where just above the midplane, but well below the photosphere, large grains can be depleted. As a result, grain sizes smaller than $\lambda / 2\pi \approx 140 \mu\text{m}$ at just above the thin midplane layer can produce the polarized flux. However, the formation of the thin dust layer may be halted by the Kelvin-Helmholtz instability; then the strong radial dependence for $\alpha = 10^{-3}$ may not appear in a realistic disk.

5.4. Alignment of grains with magnetic inclusions

We investigate how does the presence of magnetic inclusions affects on grain alignment. Figure 9 is the same as Figure 7, but for a different number of magnetic inclusions. In the presence of a modest number of magnetic inclusions and no superparamagnetic inclusions ($f_p = 0.1$, $\phi_{\text{sp}} = 0$), the figure shows grain alignment with radiative flux at the in-

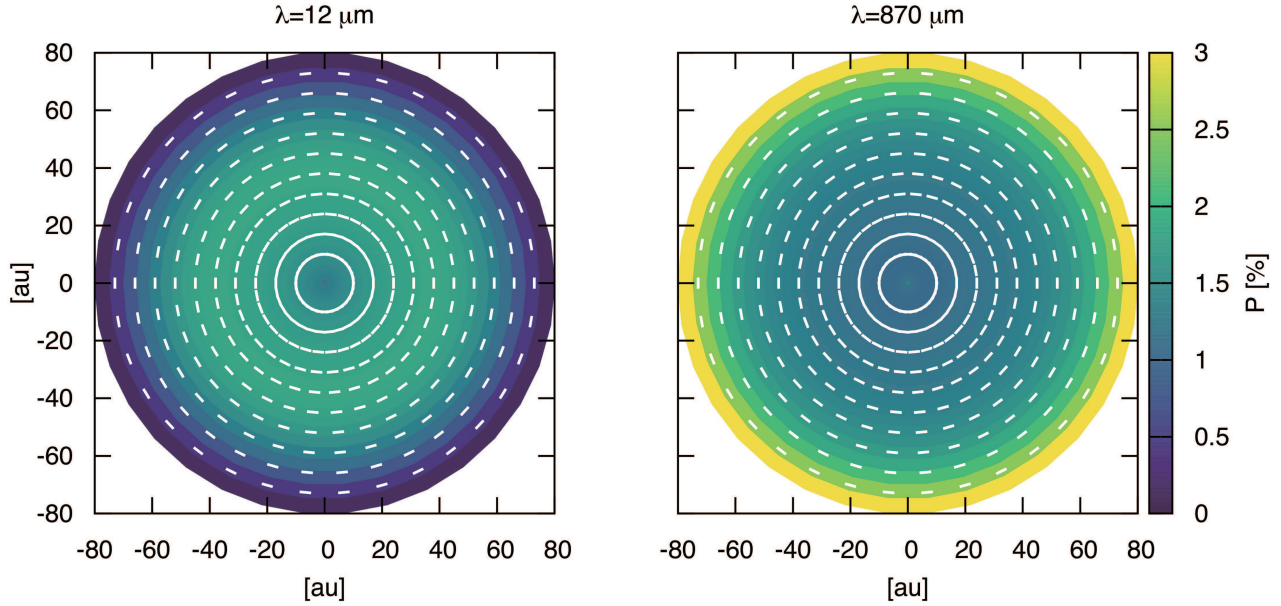


Figure 7. Polarization degree is shown with the color scale and the direction of \mathbf{E} -vector is plotted as the white bar. Left and right panels represent mid-infrared wavelength ($\lambda = 12 \mu\text{m}$) and millimeter wavelength ($\lambda = 870 \mu\text{m}$), respectively. The dust grains are assumed to be magnetically poor ($f_p = 0.01$ and $\phi_{sp} = 0$). The maximum grain size is $a_{\text{max}} = 1000 \mu\text{m}$. Turbulent strength and the $f_{\text{high-}J}$ -parameter are assumed to be $\alpha = 10^{-3}$ and $f_{\text{high-}J} = 0.5$, respectively.

ner disk, and with the magnetic field at the outer disk at mid-infrared wavelength. At the outer disk where larger grains settle down to the midplane, mid-infrared polarized emission mainly arises from surface sub-micron grains and they are aligned with respect to the magnetic field. On the other hand, at the inner disk, micron-sized grains being aligned with the radiative flux are present at the disk surface layer. Since micron-sized grains dominate the opacity at mid-infrared, we observe the azimuthal polarization vector. As a result, we see alignment with the radiation direction at the inner disk and with the magnetic field at the outer disk. When we increase the number of magnetic inclusions, the boundary radius between the radial and the azimuthal polarization vectors decreases. This is because increasing the number of magnetic inclusions increases the maximum grain size aligned with magnetic field. It should be noted that in this case, the disk polarization is less than 1%, while Figure 7 shows a larger polarization degree. This is because the direction of the radiation anisotropy is perpendicular to the toroidal magnetic field; hence, the emission arising from grains aligned with the magnetic field depolarizes the emission arising from grains aligned with the direction of radiation.

In the presence of superparamagnetic inclusions ($f_p = 0.1$, $\phi_{sp} = 0.03$), dust grains align with the magnetic field all over the disk at mid-infrared.

At millimeter wavelength, even in the presence of superparamagnetic inclusions, dust grains become aligned with the radiation direction, not with the magnetic field as one can be expected from Figure 5.

5.5. Grain size and wavelength dependence

Figure 10 shows the degree of polarization against the maximum grain size assuming $f_{\text{high-}J} = 0.5$. The degree of polarization is integrated over the whole radius of the disk. At $\lambda = 850 \mu\text{m}$, with increasing the maximum grain size, the degree of polarization decreases. This is because grains larger than the observing wavelength radiate unpolarized light; hence, with increasing the maximum grain size, more grains emit

unpolarized light, and then the degree of polarization is reduced. At mid-infrared wavelength, only (sub-)micron-sized grains at the surface layer contribute to the polarized emission because the disk is optically thick. As a result, the maximum grain size does not strongly affect on the resultant polarization degree. This result implies that as the grain growth occurs, the degree of polarization can be small at all wavelengths, in particular for the (sub-)mm. The expected degree of polarization is much smaller than that presented in CL07, who show a 36% of degree of polarization for $a_{\text{max}} = 100 \mu\text{m}$ which drops to 8% for $a_{\text{max}} = 1000 \mu\text{m}$ at $\lambda = 850 \mu\text{m}$. This difference is mostly due to the fact that CL07 assumed perfect internal alignment.

Figure 11 shows the wavelength dependence of the degree of polarization assuming the maximum grain size to be $1000 \mu\text{m}$. At around $\lambda = 40 \mu\text{m}$, a strong feature appears corresponding to the ice, where refractive index changes significantly. At millimeter wavelength, the degree of polarization increases with increasing wavelength because more larger grains can contribute to the polarized emission for a long observing wavelength. The observed degree of polarization depends on the parameter of $f_{\text{high-}J}$. If 90 % of the grains become aligned with low- J attractors, then the degree of polarization will be less than 1 % at all wavelengths. This is because at low- J attractors, internal alignment of the grains is poor, and then the degree of alignment is reduced significantly.

6. DISCUSSION

6.1. Constraint on magnetic field strength

As was discussed in Lazarian (2007) the transition from the grain alignment with respect to radiative flux to that with respect to magnetic field can be a way of determining the magnetic field (see A. Lazarian & T. Hoang 2017, in preparation). Using this approach we can place an upper limit on the magnetic field strength if we know the radiation field, and also know that the dust is aligned with respect to the radiation. Using Equations (7 and 18), the Larmor precession timescale

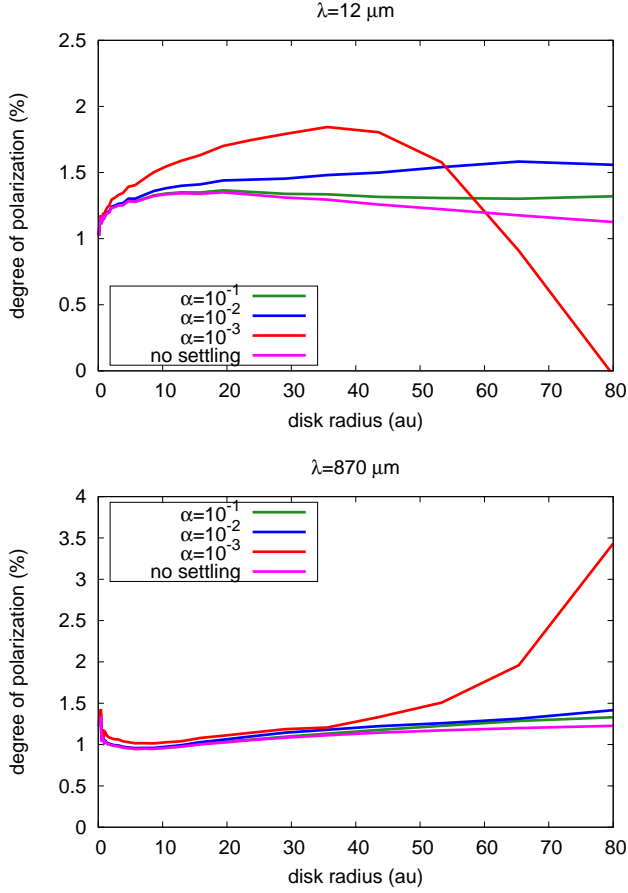


Figure 8. Degree of polarization against disk radius. The turbulent strength is varied, but the other parameters are the same as Figure 7. Top and bottom panels indicate mid-infrared wavelength ($\lambda = 12 \mu\text{m}$) and millimeter wavelength ($\lambda = 870 \mu\text{m}$), respectively. Red, blue, and green lines represent the results for different α -values, $\alpha = 10^{-3}$, 10^{-2} , and 10^{-1} , respectively, and the magenta line represents the no-settling model.

becomes longer than the radiative precession timescale when

$$B \leq 59 \text{ nG } a_{-5}^{\frac{3}{2}} \hat{\chi}^{-1} \left(\frac{\bar{\lambda}}{1.2 \mu\text{m}} \right) \left(\frac{u_{\text{rad}}}{u_{\text{ISRF}}} \right) \left(\frac{\gamma |\mathbf{Q}_r|}{0.01} \right) \quad (71)$$

It is found that when $u_{\text{rad}} = u_{\text{ISRF}}$, grain alignment with radiation direction occurs when the magnetic field strength is less than 59 nG, which is much smaller than the typical value of magnetic field strength in the ISM, $\approx \mu\text{G}$. Hence, in the ISM, dust grains become aligned with the magnetic field. At the disk surface, the energy density of the radiation is dominated by the stellar radiation; hence, substituting Equation (50) into Equation (71), we obtain

$$B \leq 0.36 \text{ G } a_{-5}^{\frac{3}{2}} \hat{\chi}^{-1} \left(\frac{\bar{\lambda}}{1.2 \mu\text{m}} \right) \left(\frac{R}{10 \text{ AU}} \right)^{-2} \left(\frac{\gamma |\mathbf{Q}_r|}{0.01} \right) \quad (72)$$

We comment on the possibility of grain alignment with respect to the magnetic field at the disk midplane. At the midplane, the wavelength of the radiation field and the grain size become much larger than the surface layer, so it is more difficult for grains to be aligned with the magnetic field. For example, when we consider the midplane at $R = 50 \text{ au}$ of the disk, the characteristic quantities of the radiation field of our disk model are $u_{\text{rad}} \approx 1.55 \times 10^{-10} \text{ erg cm}^{-3}$, $\bar{\lambda} \approx 137 \mu\text{m}$,

and $\gamma = 1$ (see Figure 4). Suppose the dust grains have a large number of superparamagnetic inclusions ($\phi_{\text{sp}} = 3 \%$ and $N_{\text{cl}} = 10^5$), and mm-sized grains; hence we can set $Q_r = 0.4$, and the grains can be aligned with the magnetic field when $B > B_{\text{crit}} = 134 \text{ mG}$ at $R = 50 \text{ au}$. The magnetic field strength adopted in this paper is $4 \times 10^{-2} \text{ mG}$ at $R = 50 \text{ au}$. Even if the toroidal magnetic field strength is amplified by 10 times, it is still too weak for grains to be aligned with respect to the magnetic field. It should also be stressed that, as shown in Figure 5, the gaseous damping timescale is often shorter than the Larmor precession timescale, i.e., mm-sized grains; hence, one should also check this point whenever grain alignment with the B -field is assumed in disks (see Equation 51).

6.2. Effect of disk inclination

In this work, we have only considered the case of face-on disks. However, most protoplanetary disks are inclined to the observer; hence, it is important to consider what happens for inclined disks (Figure 12).

Suppose the dust grains are aligned with the toroidal magnetic field; then the polarization vector (E-vector) would be radial for a face-on disk. For inclined disks, the disk is more polarized along its minor axis and the polarization vector is parallel to this axis (Figure 12, see also CL07). Along the major axis, the degree of polarization is low because the apparent shape of the oblate approaches that of a sphere.

If the dust grains align with the anisotropic radiation field, the azimuthal polarization vector can be observed for face-on disks. For inclined disks, the disk is more polarized along its major axis, and the polarization vector would be parallel to this axis. This tendency is qualitatively similar to the observation of HL Tau by CARMA (Stephens et al. 2014). It should be mentioned that the polarization pattern of HL Tau can also be explained by the self-scattering (Kataoka et al. 2016a; Yang et al. 2016a,b).

6.3. Scattering by aligned grains: circular polarization

Circular polarization can be produced by light scattering off aligned grains (see Lazarian 2007, and references therein). In this case, we expect circular polarization from disks. Circular polarization occurs by (i) scattering of aligned grains, (ii) multiple scattering, or (iii) optically active chirality. Since we are addressing emission of dust grains that are not optically active chiral, we discuss (i) and (ii) here.

The state of polarization of light is specified by four Stokes parameters, I, Q, U, V (e.g., Bohren & Huffman 1983). Upon scattering, the Stokes parameters are changed according to the scattering matrix (or Muller matrix),

$$\begin{pmatrix} I_{\text{sca}} \\ Q_{\text{sca}} \\ U_{\text{sca}} \\ V_{\text{sca}} \end{pmatrix} = \frac{1}{k^2 r^2} \begin{pmatrix} S_{11} & S_{12} & S_{13} & S_{14} \\ S_{21} & S_{22} & S_{23} & S_{24} \\ S_{31} & S_{32} & S_{33} & S_{34} \\ S_{41} & S_{42} & S_{43} & S_{44} \end{pmatrix} \begin{pmatrix} I_{\text{inc}} \\ Q_{\text{inc}} \\ U_{\text{inc}} \\ V_{\text{inc}} \end{pmatrix}, \quad (73)$$

For aligned grains, S_{41} is not zero; hence, these grains can produce circular polarization from unpolarized light upon single scattering. On the other hand, when we consider a distribution of randomly orientated grains, e.g., non-aligned grains, a symmetric treatment of the scattering matrix can reduce the non-zero independent elements, and $S_{41} = 0$ for randomly orientated grains. As a result, these grains cannot circularly polarize the unpolarized light upon single scattering. However, even in this case, since S_{43} is not zero, multiple scattering can produce the circular polarization. This is because

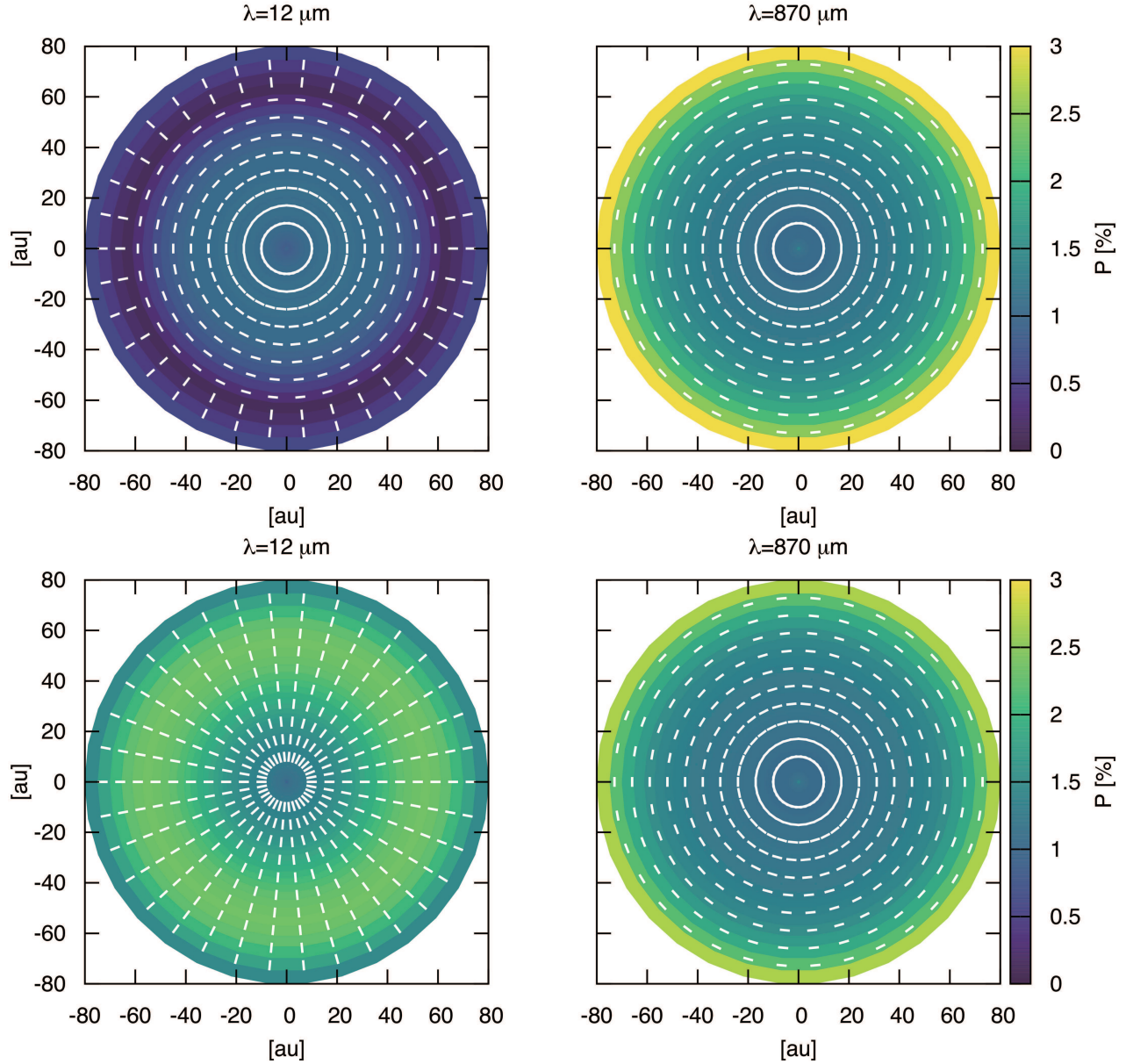


Figure 9. Same as Figure 7, but for different magnetic properties of dust. Top and bottom panels correspond to (i) moderate paramagnetic inclusion model ($f_p = 0.1$, $\phi_{sp} = 0$), and (ii) superparamagnetic inclusion model ($f_p = 0.1$, $\phi_{sp} = 0.03$, $N_{cl} = 2000$), respectively. $a_{max} = 10^3 \mu m$, $f_{high-J} = 0.5$, and $\alpha = 10^{-3}$ are assumed.

the first scattering event produces linearly polarized light, and this light is incident on other grains. The linearly polarized light ($Q \neq 0$, $U = 0$) for the first scattering coordinate can be an obliquely polarized light ($Q \neq 0$, $U \neq 0$) for the second scattering coordinate. As a result, S_{43} can produce the circular polarization by multiple scattering. Therefore, circular polarization can be produced by either single scattering by aligned grains through non-zero S_{41} , or multiple scattering by randomly orientated grains through S_{43} . Since, at millimeter wavelength, protoplanetary disks are often optically thin, multiple scattering may not be important for many cases. Hence, we focus on the circular polarization due to scattering by aligned grains.

In the Rayleigh limit (dipole approximation), the scattering matrix of an ellipsoid can be written as (e.g., Bandermann & Kemp 1973; Dolginov et al. 1978;

Gledhill & McCall 2000)

$$S_{41} = \frac{1}{2} ik^6 (\alpha_1 \alpha_3^* - \alpha_1^* \alpha_3) [(\vec{e}_0 \times \vec{e}_1] \cdot \hat{a}_1) (\vec{e}_0 \cdot \hat{a}_1) \quad (74)$$

where \vec{e}_0 and \vec{e}_1 are the incident light and scattered light directions; hence these two vectors define the scattering plane. α is the polarizability of an ellipsoid with respect to each axis, given by Equation (54). We can see from Equation (74) that we do not expect circular polarization for (i) non-absorbing particles ($\text{Im}(\alpha) \neq 0$), (ii) forward scattering and backward scattering, (iii) grains' minor axis being in the scattering plane ($[(\vec{e}_0 \times \vec{e}_1] \cdot \hat{a}_1) = 0$), and (iv) grains' minor axis being perpendicular to the incident radiation.

Imaging observations of protoplanetary disks at visible/near-infrared wavelengths is dominated by the scattered light from disks. Since dust grains at the surface

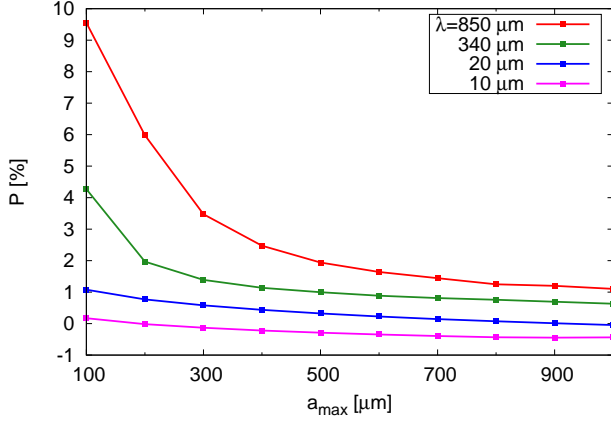


Figure 10. Degree of polarization as a function of maximum grain size. Red, green, blue, and magenta lines indicate the result at $\lambda = 870 \mu\text{m}$, $\lambda = 340 \mu\text{m}$, $\lambda = 20 \mu\text{m}$, and $\lambda = 10 \mu\text{m}$, respectively. Positive and negative values represent the alignment with radiation direction and magnetic field, respectively.

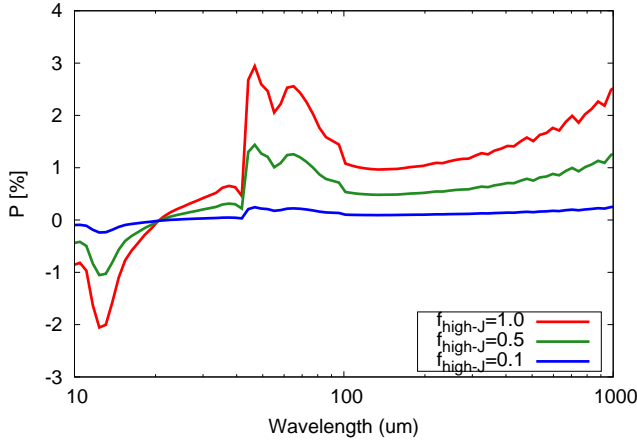


Figure 11. Degree of polarization against wavelength. Red, green, and blue lines indicate $f_{\text{high-J}} = 1.0, 0.5$, and 0.1 , respectively.

layer are exposed to the stellar radiation, we can expect grain alignment with the radiation direction or with the magnetic field. The degree of linear polarization can be high due to the scattering polarization, and then the polarized thermal emission is hardly detectable. However, still in this case, we can still expect the circular polarization from visible/NIR imaging. In the solar-system, it is known that the zodiacal light is circularly polarized, and this has been explained as due to scattering by aligned grains (e.g., Dolginov et al. 1978; Hoang & Lazarian 2014). The observation of the circular polarization in the visible/NIR may help to constrain RAT alignment in protoplanetary disks.

6.4. Implications for Millimeter-wave Polarization

We summarize what we can learn from the millimeter-wave polarization observations for ALMA Era.

A radially aligned polarization vector is expected for grain alignment with the toroidal magnetic field (CL07; Yang et al. 2016a,b; Matsakos et al. 2016; Bertrang et al. 2017). For small grains compared to the radiation wavelength, RAT becomes inefficient, and then RAT alignment does not occur. For large grains, the Larmor precession timescale is often

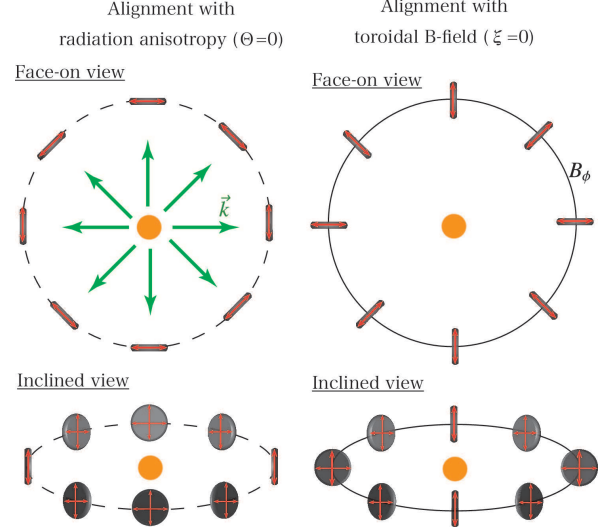


Figure 12. Schematic illustration of the polarization vector arising from aligned grains. Left and right panels show the case of alignment with radiation direction and toroidal magnetic field, respectively. Top and bottom panels show face-on views and inclined view of the disk. Red arrows denote the E-vector. In this illustration, perfect internal alignment ($\theta = 0$) is assumed.

longer than the gaseous damping timescale. Even if Larmor precession overcomes the gaseous damping, grain alignment with the magnetic field does not occur unless the Larmor precession timescale becomes shorter than the radiative precession timescale. This suggests that the a required magnetic field strength for B -alignment is quite strong and dust grains should have large numbers of superparamagnetic inclusions (see Equation 71). Hence, if ALMA finds the signature of the alignment with the magnetic field, this implies that the magnetic field strength in the disk might be stronger than expected so far.

If we observe a polarization vector which is consistent with alignment with the radiative flux, there are two possibilities, (i) self-scattering (Kataoka et al. 2015) and/or (ii) grain alignment with the radiation direction (Figure 7 or Figure 9). For self-scattering, we can constrain on the grain size as discussed by Kataoka et al. (2015). For grain alignment, we can constrain the upper limit on the magnetic field strength. In addition, the efficiency of RAT depends on the grain shape and size, and it might be possible to constrain grain properties. How can we distinguish between self-scattering and grain alignment observationally? As discussed in Section 6.3, if self-scattering and grain alignment occur simultaneously, we expect circular polarization from disks. If disks do not show circularly polarized emission, disentangling between them becomes more challenging. One way to distinguish between them is to observe the degree of linear polarization. For the self-scattering scenario, the degree of polarization is proportional to the radiation anisotropy at millimeter wavelength, hence it might be inferred from intensity observation. The degree of polarization due to grain alignment is determined by the grain axis ratio and the alignment efficiency. As shown in Figure 6, the axis ratio can increase the polarization degree. Hence, if we observe a much larger polarization degree than that estimated from the anisotropy of the radiation field, grain alignment might explain this. It is worth noting that, in principle, grain alignment is determined by the radiation anisotropy of radiation field *integrated over all wavelengths*,

while millimeter scattering traces the anisotropy at *millimeter wavelength*. These two radiation fields are not necessary the same. Another solution is to perform multi-wavelength observations, because the polarized intensity due to self-scattering shows a maximum value at $\lambda_{\text{obs}} \approx 2\pi a_{\text{max}}$, and otherwise polarization intensity drops quickly to zero (Kataoka et al. 2015), while grain alignment predicts weaker wavelength dependence.

Recently, the first submillimeter polarization observation by ALMA was reported by Kataoka et al. (2016b). The disk shows the radial polarization vector, and the polarization vector flips by 90° at its edge. They performed radiative transfer modeling of this object, taking self-scattering into account. They found that the self-scattering model succeeded in reproducing the radial polarization vector as well as the flip of polarization vectors at the edge of the disk. Since this disk has a ring-like structure, and at the center of the ring, the radiative flux can be in the azimuthal direction, and then the scattering can produce the radial polarization vector (e.g., Kataoka et al. 2015). The flip of the polarization vector also be naturally explained by the change of the direction of the radiative flux. On the other hand, the self-scattering model does not reproduce the highest polarization region where the polarization degree is 13.9 %. According to the RAT alignment we studied in this paper, dust grains are likely to be aligned with the direction of radiative flux at (sub-)millimeter wavelength. Hence, even if we consider the RAT alignment, the observed polarization pattern of HD 142527 might be reproduced including the flip of the polarization vector. One advantage of the grain alignment model is that alignment polarization might explain the highest polarization region of HD 142527. More detailed modeling of this object taking the grain alignment into account will be left for the future study.

7. SUMMARY

We applied RAT theory of grain alignment to protoplanetary disks. Our findings can be summarized as follows.

- Near the star the RAT alignment is expected in the direction determined by the radiation flux rather than the magnetic field. The dust grains are expected to become aligned with their short axis to the radiation direction. If radiative alignment is taken into account, millimeter wavelength polarization can be arose from aligned grains, and the polarization vector traces the direction of radiation anisotropy.
- Large grains in disks may not be aligned with the magnetic field as their precession rate may be less than the Larmor precession or the precession in the magnetic field. Therefore polarimetry can test the percentage of such grains.
- Smaller grains may align with the magnetic field at low-density regions such as the surface layer, and this might be observed in the mid-infrared polarimetry of disks. The magnetic field alignment at the surface layer occurs when dust grains have superparamagnetic inclusions or the disk magnetic field is strong (Equation 72).
- The degree of millimeter-wave polarization depends mainly on maximum grain size a_{max} , axis ratio s , and $f_{\text{high-J}}$. For $a_{\text{max}} = 100 \mu\text{m}$, we expect $P \approx 10\%$ polarization degree, but for $a_{\text{max}} = 1000 \mu\text{m}$ the polarization degree drops to $P \approx 1\%$.

- The degree of mid-infrared polarization mainly depends on the magnetic susceptibility at zero frequency $\chi(0)(f_p \text{ and } \phi_{\text{sp}})$, axis ratio s , and $f_{\text{high-J}}$. The radial dependence of mid-infrared polarization is sensitive to the strength of turbulent.

We appreciate useful comments by the referee. R.T. is supported by the Research Fellowship from JSPS for Young Scientists (15J02840). A.L. acknowledges NSF grant AST 1109295, NASA grant NNH 08ZDA0090. This work was supported by Grants-in-Aid for Scientific Research 23103005 and 25400229, and the International collaboration program at Tokyo Tech (HN). R.T. thanks to Akimasa Kataoka, C. P. Dullemond, Hidekazu Tanaka, and Satoshi Okuzumi for useful discussions.

REFERENCES

- Andersson, B.-G., Lazarian, A., & Vaillancourt, J. E. 2015, ARA&A, 53, 501
- Balbus, S. A., & Hawley, J. F. 1991, ApJ, 376, 214
- Bandermann, L. W., & Kemp, J. C. 1973, MNRAS, 162, 367
- Barnett, S. J. 1915, Physical Review, 6, 239
- Bertrang, G. H.-M., Flock, M., & Wolf, S. 2017, MNRAS, 464, L61
- Bohren, C. F., & Huffman, D. R. 1983, Absorption and scattering of light by small particles (New York: Wiley)
- Bradley, J. P. 1994, Science, 265, 925
- Chandrasekhar, S. 1960, Proceedings of the National Academy of Science, 46, 253
- Cho, J., & Lazarian, A. 2007, ApJ, 669, 1085 (CL07)
- Cox, E. G., Harris, R. J., Looney, L. W., et al. 2015, ApJ, 814, L28
- Davis, L. J., & Greenstein, J. L. 1951, ApJ, 114, 206
- Dolginov, A. Z., & Mitrofanov, I. G. 1976, Ap&SS, 43, 291
- Dolginov, A. Z., Mitrofanov, I. G., & Mytrophanov, I. G. 1978, A&A, 69, 421
- Draine, B. T. 1996, in Astronomical Society of the Pacific Conference Series, Vol. 97, Polarimetry of the Interstellar Medium, ed. W. G. Roberge & D. C. B. Whittet, 16
- Draine, B. T. 2011, Physics of the Interstellar and Intergalactic Medium (PRINCETON UNIVERSITY PRESS)
- Draine, B. T., & Flatau, P. J. 1994, J. Opt. Soc. Am. A, 11, 1491
- Draine, B. T., & Lazarian, A. 1998, ApJ, 508, 157
- Draine, B. T., & Lee, H. M. 1984, ApJ, 285, 89
- Draine, B. T., & Weingartner, J. C. 1996, ApJ, 470, 551
- Draine, B. T., & Weingartner, J. C. 1997, ApJ, 480, 633
- Flock, M., Ruge, J. P., Dzyurkevich, N., et al. 2015, A&A, 574, A68
- Gledhill, T. M., & McCall, A. 2000, MNRAS, 314, 123
- González-Casanova, D. F., Lazarian, A., & Santos-Lima, R. 2016, ApJ, 819, 96
- Henning, T., & Stognienko, R. 1993, A&A, 280, 609
- Hildebrand, R. H., & Dragovan, M. 1995, ApJ, 450, 663
- Hoang, T., & Lazarian, A. 2008, MNRAS, 388, 117
- Hoang, T., & Lazarian, A. 2009a, ApJ, 697, 1316
- Hoang, T., & Lazarian, A. 2009b, ApJ, 695, 1457
- Hoang, T., & Lazarian, A. 2014, MNRAS, 438, 680
- Hoang, T., & Lazarian, A. 2016, ArXiv e-prints, arXiv:1605.02828
- Hughes, A. M., Hull, C. L. H., Wilner, D. J., & Plambeck, R. L. 2013, AJ, 145, 115
- Hughes, A. M., Wilner, D. J., Cho, J., et al. 2009, ApJ, 704, 1204
- Jones, R. V., & Spitzer, L. J. 1967, ApJ, 147, 943
- Kataoka, A., Muto, T., Momose, M., Tsukagoshi, T., & Dullemond, C. P. 2016a, ApJ, 820, 54
- Kataoka, A., Muto, T., Momose, M., et al. 2015, ApJ, 809, 78
- Kataoka, A., Tsukagoshi, T., Momose, M., et al. 2016b, ApJ, 831, L12
- Kim, S.-H., & Martin, P. G. 1995, ApJ, 444, 293
- Landau, L. D., & Lifshitz, E. M. 1960, Electrodynamics of continuous media (Oxford: Pergamon Press)
- Laor, A., & Draine, B. T. 1993, ApJ, 402, 441
- Lazarian, A. 2005, in American Institute of Physics Conference Series, Vol. 784, Magnetic Fields in the Universe: From Laboratory and Stars to Primordial Structures., ed. E. M. de Gouveia dal Pino, G. Lugones, & A. Lazarian, 42–53

- Lazarian, A. 2007, *J. Quant. Spec. Radiat. Transf.*, 106, 225
- Lazarian, A. 2014, *Space Sci. Rev.*, 181, 1
- Lazarian, A., Andersson, B.-G., & Hoang, T. 2015, *Polarimetry of Stars and Planetary Systems*, 81
- Lazarian, A., & Draine, B. T. 1999, *ApJ*, 520, L67
- Lazarian, A., & Draine, B. T. 1999, *ApJ*, 516, L37
- Lazarian, A., & Efrogmsky, M. 1999, *MNRAS*, 303, 673
- Lazarian, A., & Hoang, T. 2007, *MNRAS*, 378, 910 (LH07)
- Lazarian, A., & Hoang, T. 2008, *ApJ*, 676, L25
- Lazarian, A., & Roberge, W. G. 1997, *ApJ*, 484, 230
- Lee, H. M., & Draine, B. T. 1985, *ApJ*, 290, 211
- Li, D., Pantin, E., Telesco, C. M., et al. 2016, *ApJ*, 832, 18
- Li, Z.-Y., Banerjee, R., Pudritz, R. E., et al. 2014, *Protostars and Planets VI*, 173
- Lynden-Bell, D., & Pringle, J. E. 1974, *MNRAS*, 168, 603
- Martin, P. G. 1971, *MNRAS*, 153, 279
- Martin, P. G. 1995, *ApJ*, 445, L63
- Mathis, J. S., Mezger, P. G., & Panagia, N. 1983, *A&A*, 128, 212
- Matsakos, T., Tzeferacos, P., & Königl, A. 2016, *MNRAS*, 463, 2716
- Miyake, K., & Nakagawa, Y. 1993, *Icarus*, 106, 20
- Morrish, A. H. 2001, *The Physical Principles of Magnetism* (Wiley-IEEE Press), 696
- Okuzumi, S., Takeuchi, T., & Muto, T. 2014, *ApJ*, 785, 127
- Pohl, A., Kataoka, A., Pinilla, P., et al. 2016, *A&A*, 593, A12
- Purcell, E. M. 1979, *ApJ*, 231, 404
- Purcell, E. M., & Spitzer, Jr., L. 1971, *ApJ*, 167, 31
- Rao, R., Girart, J. M., Lai, S.-P., & Marrone, D. P. 2014, *ApJ*, 780, L6
- Roberge, W. G., Degraff, T. A., & Flaherty, J. E. 1993, *ApJ*, 418, 287
- Stephens, I. W., Looney, L. W., Kwon, W., et al. 2014, *Nature*, 514, 597
- Velikhov, E. P. 1959, *Soviet Physics JETP*, 36, 995
- Weingartner, J. C., & Draine, B. T. 2003, *ApJ*, 589, 289
- Yang, H., Li, Z.-Y., Looney, L., & Stephens, I. 2016a, *MNRAS*, 456, 2794
- Yang, H., Li, Z.-Y., Looney, L. W., et al. 2016b, *MNRAS*, 460, 4109
- Youdin, A. N., & Lithwick, Y. 2007, *Icarus*, 192, 588